

Direct electrical modulation of surface response in a single plasmonic nanoresonator

Luka Zurak,^{1,*} Christian Wolff,² Jessica Meier,¹ René Kulloock,¹ N. Asger Mortensen,^{2,3} Bert Hecht,¹ and Thorsten Feichtner^{1,†}

¹*Nano-Optics and Biophotonics Group, Experimental Physics 5,
Institute of Physics, University of Würzburg, Germany*

²*POLIMA – Center for Polariton-driven Light-Matter Interactions,
University of Southern Denmark, Campusvej 55, DK-5230 Odense M, Denmark*

³*Danish Institute for Advanced Study, University of Southern Denmark, Campusvej 55, DK-5230 Odense M, Denmark*

Classical electrodynamics describes the optical response of systems using bulk electronic properties and treats boundaries between two materials as infinitesimally thin. However, due to the quantum nature of electrons, interfaces have a finite thickness. Non-classical surface effects become increasingly important as ever smaller nanoscale systems are realized and eventually dominate over volume-related phenomena. Investigating the response of surface electrons in such systems, therefore, becomes imperative. One way to gain control over non-classical interface effects and study them is through electrical gating, as the static screening charges reside exclusively at the surface. Here, we investigate the modulation of the surface response upon direct electric charging of a single plasmonic nanoresonator by measuring the resulting changes in resonance. We analyze the observed effects within the general framework of surface-response functions and provide a basic model derived from electron spill-out within the local-response approximation (LRA). Our observed change in resonance frequency is well accounted for by assuming a modulation of the in-plane surface current. Surprisingly, we also measure a change in the resonance width, where adding electrons to the surface leads to a narrowing of the plasmonic resonance, i.e., reduced losses. The description of such effects requires considering nonlocal effects and the inclusion of a possible anisotropy of the perturbed surface permittivity. Our experiment, therefore, opens a vast field of investigations on how to gain control over the surface response in plasmonic resonators and to develop ultrafast and extremely small electrically driven plasmonic modulators and metasurfaces by leveraging electrical control over non-classical surface effects.

I. Introduction

The interaction between free electrons at a metal surface and electromagnetic fields at optical frequencies gives rise to surface plasmon polaritons (SPPs), which are strongly coupled states of light and charge-density oscillations [1]. When SPP waves are confined to finite-sized objects, they exhibit resonances with large field enhancements in the vicinity of maxima in the surface-charge density [2]. By tailoring the

geometry of the object, one can effectively control and adjust the spectral position of the SPP resonances [3]. These practical properties of localized plasmonic resonances have been extensively studied and widely utilized [4–9]. However, the lack of possibilities to *actively* tune plasmonic resonances still remains a major obstacle in realizing the full potential of plasmonic systems. Active tuning would enable the development of ultrafast and ultrasmall optical modulators and tunable metamaterials [10]. At the first glance, one of the most compelling pathways towards dynamic tuning is varying the density of the electron gas. This feature is already exploited in dilute systems, such as graphene plasmonics [11–13], but often disregarded in metallic nanoresonators with higher carrier densities. To investigate the tuning of plasmonic nanoresonators various methods have been employed for enhancing the electrical charging, such as embedding resonators in a chemical reductant or an ion gel, which has resulted in a significant increase in the capacitance of the system [14–25]. However, these approaches have severe limitations, including slow operation and inconclusive results. Hysteresis has been observed in some cases, likely due to double-layer formation or electrochemical reactions at the metal surface, suggesting different origins of the observed tuning effects beyond pure charging. Consequently, there is a necessity to carry out experiments free from the potential impacts of environmental variations by means of direct electrical charging.

On the theoretical side a common approach in modeling of observed resonance changes is based on the incorrect assumption that electrostatic charges lead to a change in the bulk properties [15, 16, 26]. Only few studies have explored the impact of charging on the optical response, viewing it as a surface-related phenomenon [21, 23, 27–29]. Among these, Brown *et al.* utilize a core-shell model, offering only a simplistic explanation and, consequently, limited insights into the optical characteristics of electrons at the surface [21]. While Hoener *et al.* did develop a more advanced semi-classical model based on electron spill-out, it ultimately resulted in a debated interpretation of the experimental observations [23]. In the latest developments, Li *et al.* have examined the resonance of a nanoscale electron reservoir placed within a narrow plasmonic gap using a quantum hydrodynamic model [29]. Their theoretical findings show enormous potential, emphasizing the possibility to obtain large resonance modulation driven by a strong perturbation of the out-of-plane surface electron response, while neglecting the in-plane response. We conclude that a universal framework and a simple analytical model, to treat changes of the optical response of plasmonic nanoresonators upon charging, is unavailable. In particular,

* luka.zurak@physik.uni-wuerzburg.de

† thorsten.feichtner@physik.uni-wuerzburg.de

taking into account the full non-classical properties of electrons at the surface, remains a challenge. It is no coincidence that more recently, the further development of a framework to describe the optical response of electrons at the surface of metals has gained much attention, as non-classical surface properties have been found to strongly shape the response of nanoscale plasmonic systems [30–41]. Reduced field enhancement, accompanied by broadening and spectral shifting of resonances, are caused by electronic spill-out [39, 42], non-locality [43], and Landau damping [44–46], effects which can be treated using the universal framework of surface-response functions, better known as Feibelman d -parameters [40].

As nanofabrication and computational methods continue to progress, the potential and importance of smaller nanoresonators with pronounced surface effects are increasing, bridging the divide between classical and quantum facets of linear and nonlinear optical responses. Therefore, conducting experiments that employ direct electrical charging and evaluating the results within the framework of surface-response functions can contribute to a deeper understanding, ultimately facilitating the enhancement of electrical tuning in smaller systems where surface effects play a dominant role. Moreover, the appearance of an inverse optoelectronic effect, referred to as the plasmoelectric potential, hinges fundamentally on the electrical tunability of plasmonic resonances [26].

In this study, we experimentally investigate the effect of direct electrical charging on the fundamental dipolar resonance of a single plasmonic nanoresonator (as sketched in Fig. 1a), while carefully excluding slow phenomena typically associated with electrochemical processes. To this end, we measure the relative change in light scattering for applied electric potentials of up to ± 20 V, from which we determine the induced changes in the nanoresonator’s eigenfrequency and line width. We place the observed changes within the general framework of surface-response functions for which we provide a basic model derived from electron spill-out in local-response approximation (LRA). The observed shift in the resonance frequency can be nicely explained by a modulation of the in-plane surface response. However, we also observe a change in the resonance width, which is in stark contrast with the predictions of our model. To account for this observation the basic assumptions of our model need to be extended likely towards anisotropy of the local permittivity, the perturbation of conductivity via surface-states, or nonlocal effects hidden in the perpendicular component of the d -parameters.

II. Surface-response functions

Bohren and Hunt [27] made one of the initial attempts to model how adding electrons to the surface of a plasmonic nanoresonator affects the resonance. They assumed that, in the picture of classical electrodynamics, added electrons modify the surface conductivity σ_s and consequently perturb the in-plane surface current $\mathbf{K} = \sigma_s \mathbf{E}_{\parallel}$ driven by the tangential component of electric field \mathbf{E}_{\parallel} yielding a change in the effective plasma frequency (see Supplementary Section 1.1). However, to fully capture the optical properties of electrons at the surface one has to take into account vari-

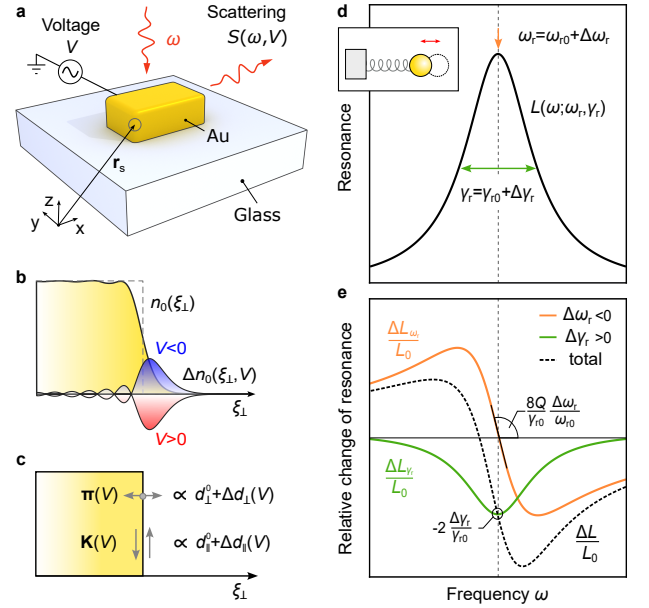


FIG. 1. **Influence of electrostatically induced surface charges on optical response of plasmonic nanoresonators.** **a**, Sketch of the system under research; a rectangular gold (Au) nanoresonator is placed on top of a glass substrate. The applied electric potential V induces a change in the resonance which is detected by recording the scattering signal $S(\omega, V)$ as a function of the photon energy $\hbar\omega$ and the applied potential. **b**, Equilibrium and induced electron density distributions at the gold-air interface calculated using a Wigner–Seitz radius of $r_s/a_0 = 3.18$ in the jellium description. Grey-dashed line denotes the position of a positive background. **c**, The change in electron density at the surface position \mathbf{r}_s perturbs the d -parameters, and in turn the optical response of the system by altering the surface polarization $\mathbf{P}_s(V)$ (see Eq. (2)). **d**, Model of a harmonic oscillator and a corresponding resonance curve with a Lorentzian line shape $L(\omega; \omega_r, \gamma_r)$ described by its resonant frequency ω_r and width γ_r . **e**, Small perturbations of $\Delta\omega_r < 0$, or $\Delta\gamma_r > 0$, lead to distinct relative changes of the resonance represented by the orange curve ($\Delta\omega_r$) and the green curve ($\Delta\gamma_r$), respectively. Change in resonance width is related to relative change at the resonant frequency, while change in resonance position is linked to the slope of this relative change - $Q = \omega_r/\gamma_r$ stands for the quality factor. Total change, represented by the black dashed line, is a superposition of the two.

ous non-classical effects. First of all, electron spill-out causes the surface to acquire a finite thickness (see Fig. 1b) and leads to an out-of-plane response. Other quantum effects which influence the electronic response at the surface are non-locality, Landau damping and conduction through surface-states [47, 48]. All such effects can be accounted for by Feibelman d -parameters [30, 47]. These d -parameters, d_{\perp} and d_{\parallel} , are centroids of the induced charge density and of the normal derivative of the tangential current, respectively [30] (see Supplementary Section 1.2-3). Hence, as demonstrated by Christensen *et al.* [49], d -parameters describe the surface polarization

$$\mathbf{P}_s = \boldsymbol{\pi} + i\omega^{-1}\mathbf{K}, \quad (1)$$

which can be added to the classical framework by extending the boundary conditions [40]. The out-of-plane electron oscillation, proportional to d_{\perp} , is described via the dipole density $\boldsymbol{\pi} = \varepsilon_0 d_{\perp} \Delta E_{\perp} \hat{x}_{\perp}$, where ε_0 is the free-space permittivity, E_{\perp} is the perpendicular component of electric field, and \hat{x}_{\perp} is the unit vector normal to the surface. The parallel component d_{\parallel} contributes to an in-plane surface current $\mathbf{K} = i\omega d_{\parallel} \Delta \mathbf{D}_{\parallel}$ as already discussed above, where \mathbf{D}_{\parallel} is the tangential component of the displacement field (see Fig. 1c).

If we assume a simple harmonic oscillator as a model for a plasmonic nanoresonator (see Fig. 1d), the associated Lorentzian $L(\omega; \omega_r, \gamma_r)$ can be described by a complex eigenfrequency $\tilde{\omega}_r = \omega_r - i\gamma_r/2$ [50]. The real part corresponds to the resonance frequency, while the imaginary part describes the attenuation of the system. It contains radiation as well as Ohmic losses. Surface effects described by the Feibelman d -parameters lead to a change of the plasmonic nanoresonator's complex eigenfrequency $\Delta\tilde{\omega}_r$, which is directly related to the surface polarization via the integral [51]

$$\Delta\tilde{\omega}_r = -\tilde{\omega}_{r0} \int_s \mathbf{E}^{(0)} \cdot \mathbf{P}_s^{(0)} ds, \quad (2)$$

where s denotes the surface of the resonator. Here, $\mathbf{P}_s^{(0)}$ and $\mathbf{E}^{(0)}$ are evaluated at the unperturbed complex eigenfrequency $\tilde{\omega}_{r0}$ obtained by assuming classical piecewise constant material properties, neglecting any non-classical effects introduced via the surface polarization $\mathbf{P}_s^{(0)}$. Therefore, the experimentally observed eigenfrequency of an uncharged plasmonic nanoresonator corrected by surface effects is given as a $\tilde{\omega}_r = \tilde{\omega}_{r0} + \Delta\tilde{\omega}_r$.

In the case of a controlled perturbation, the additional shift in the spectral position of the resonance frequency $\Delta\omega_r$ produces a distinct pattern in the relative change of the resonance, as depicted in Fig. 1e. It can be easily differentiated from the relative change pattern caused by a perturbation of the width of the resonance $\Delta\gamma_r$ (see Supplementary Section 1.4).

We use this formalism to investigate and describe the charge-induced eigenfrequency shifts of a single gold nanoresonator residing on top of a glass substrate (see Fig. 1a). At any point on the surface of the nanoresonator \mathbf{r}_s , an applied voltage V will introduce a change in equilibrium electron density (see Fig. 1b) and locally perturb the surface-response functions

$$\begin{aligned} d_{\perp}(\mathbf{r}_s, V) &\simeq d_{\perp}^0(\mathbf{r}_s) + \frac{\partial d_{\perp}(\mathbf{r}_s, V)}{\partial V} V, \\ d_{\parallel}(\mathbf{r}_s, V) &\simeq d_{\parallel}^0(\mathbf{r}_s) + \frac{\partial d_{\parallel}(\mathbf{r}_s, V)}{\partial V} V. \end{aligned} \quad (3)$$

Here, $d_{\perp}^0(\mathbf{r}_s)$, $d_{\parallel}^0(\mathbf{r}_s)$ are unperturbed d -parameters, typically taken to be constant across a metal-dielectric interface. The d -parameter perturbations $\Delta d_{\perp}(V)$, $\Delta d_{\parallel}(V)$ will lead to a local change of the surface polarization $\Delta \mathbf{P}_s(\mathbf{r}_s, V)$ (see Fig. 1c), which will introduce a voltage-induced change in the system's complex eigenfrequency $\Delta\tilde{\omega}_r(V)$ in accordance with Eq. (2). These changes can be detected by recording the relative change of scattering $\Delta S(V)/S_0$ (as shown in Fig. 1e), where $\Delta S(V)$ is the voltage-induced change in scattering signal and S_0 is the scattering signal of the uncharged system –

the scattering signal is defined as normalized scattering cross section $S \propto \sigma_{\text{sca}}$.

III. Experiment

To experimentally investigate the effect of charging on the plasmonic resonance, we conducted dark-field scattering measurements on electrically connected nanoresonators, as depicted in Fig. 2a. The plasmonic resonators under investigation are fabricated from 50 nm thick single crystalline gold microplatelets [52], using a two-step focused ion beam (FIB) milling process (similar to the procedure in Ref. 53). The first step involved Ga-FIB to create the rough shape of the resonator and connector. Then, He-FIB was employed to refine the structure's final shape with precision. An example of a 180 nm long nanoresonator is shown in the inset of Fig. 2b. The shape of the resonance was probed with a supercontinuum white-light laser, spectrally tuned using a narrowband filter, with its collimated beam polarized along the long-axis of the resonator (for more details see Supplementary Section 2.1). The scattering signal S is proportional to the ratio of the power scattered by the structure P and the incoming intensity I (see Supplementary Section 2.2-3). In Fig. 2b, we plot the normalized scattering spectra of 80 nm wide resonators with lengths ranging from 180 nm down to 100 nm. To retrieve the change in scattering we drive the system using a sinusoidal voltage with an amplitude V at frequency ν_0 and employ a phase-sensitive lock-in amplifier to detect both the amplitude ΔP and the phase ϕ of the voltage-modulated scattered power, as illustrated in Fig. 2a. The unperturbed scattered power P_0 was recorded using an optical powermeter placed in one of the branches of the detection system (see Supplementary Figure S4). By repeating the measurement across the spectrum for a voltage amplitude of 10 V at a linear frequency of 24 kHz, we observe a purely in-phase lock-in signal ($\phi = 0, \pi$) at the fundamental frequency for the relative change of scattering as shown in Fig. 2c (see Supplementary Section 2.4).

IV. Results and discussion

Across all nanoresonators, we consistently observe a similar spectral shape in the change of scattering, suggesting a red-shift and broadening of the resonance under positive bias, i.e. exhibiting a blue-shift and narrowing under negative bias. In contrast to classical models which predict solely a shift of the resonance frequency we observe also an influence on the resonance width, where adding electrons to the surface reduces the loss. Notably, smaller structures demonstrate a more pronounced modulation indicating a route to further increase the effect. For the exemplary case of the 140 nm long resonator, we demonstrate a linear relation between the observed changes and the applied voltage's amplitude by recording signals at three specific spectral points (see Fig. 2d). Additionally, we demonstrate that the observed changes at these three spectral points remain unaffected by the frequency of the AC signal within the observable spectral range, constrained by the responsiveness of the lock-in amplifier (see Fig. 2e). This im-

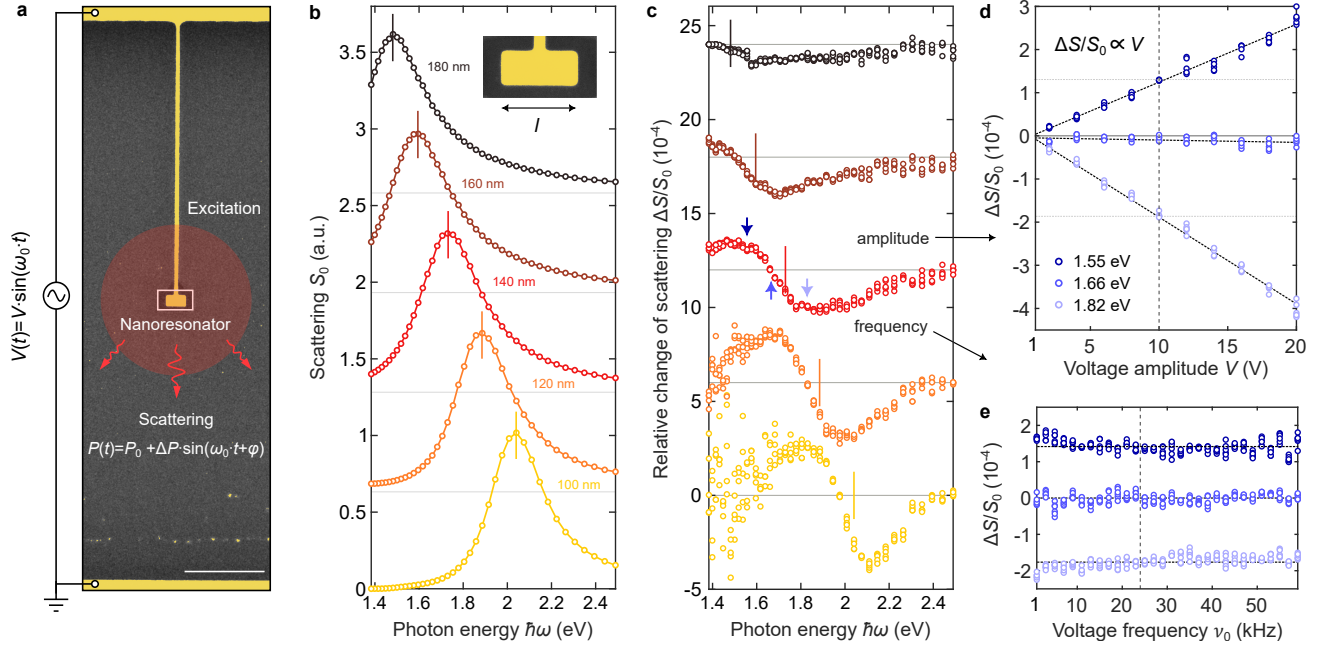


FIG. 2. **Measuring the voltage induced change of a plasmonic resonance.** **a**, Colored SEM image of a single electrically connected gold nanoresonator. The structure is driven with a sinusoidal voltage $V(t)$ while monitoring the scattered power $P(t)$. Scale bar is 500 nm. **b**, Measured scattering spectra for resonators with length ranging from 180 nm down to 100 nm - due to the small error margin, which hinders the discrimination of individual points, only one point per photon energy is plotted. The inset shows a colored close-up SEM image of the 180 nm long nanoresonator. **c**, Relative change of scattering as obtained from lock-in measurements for 10 V of voltage amplitude corresponding to the resonators in **a**. **d(e)**, Dependency of relative change of scattering on the amplitude (frequency) of the applied voltage, respectively, for three spectral points denoted in **c**.

plies that we can exclude slow processes typically encountered in the experiments performed in electrochemical cells. To get an insight into the mechanism which causes the experimentally observed resonance changes within the framework of surface-response functions, we need to determine the voltage-dependent d -parameter perturbations (see Eq. (3)).

A. Electron spill-out and local response approximation (LRA)

A complete analysis in determining d -parameter perturbations would encompass all possible microscopic phenomena taking place at the surface of the charged nanoresonator. Here, in a first approximation, we calculate the perturbation coefficients $\partial_V d_\perp$ and $\partial_V d_\parallel$, as a function of the position on the surface \mathbf{r}_s , resulting solely from the electron spill-out under the LRA. We assume a position-dependent plasma frequency $\omega_p(\xi_\perp, V) = \omega_{p0} \sqrt{n_0(\xi_\perp, V)/n_0}$, where ω_{p0} is the unperturbed plasma frequency, $n_0(\xi_\perp, V)$ is voltage-dependent equilibrium electron density, n_0 is the bulk density of free electrons and ξ_\perp parameterizes the distance perpendicular to the interface to capture e.g. the electron spill-out. In this approximation, the optical properties are then described by a position-dependent local permittivity (see Fig. 3a)

$$\epsilon_{\text{LRA}}(\xi_\perp, V) = \epsilon_b(\xi_\perp) - \frac{\omega_{p0}^2}{\omega^2 + i\gamma\omega} \frac{n_0(\xi_\perp) + \Delta n_0(\xi_\perp, V)}{n_0}, \quad (4)$$

where $n_0(\xi_\perp)$ is the equilibrium electron density of an uncharged system and $\Delta n_0(\xi_\perp, V)$ is the voltage-induced electron density (see Fig. 1d). $\epsilon_b(\xi_\perp)$ is the position dependent background permittivity which in bulk gold is dominated by interband contribution while outside the gold it transitions to the permittivity of the surrounding dielectric. For simplicity, we assume that the electron response at any point at the surface is isotropic, although it is expected that the equation-of-motion perpendicular to the interface contains additional terms that describe the influence of the boundary. Within these assumptions, according to Ref. 42, the d -parameter perturbation coefficients can be expressed in integral form as

$$\frac{\partial d_\perp}{\partial V} = \frac{\epsilon_d \epsilon_m}{\epsilon_m - \epsilon_d} \int_{-\infty}^{\infty} d\xi_\perp \frac{1}{\epsilon_{\text{LRA}}^2(\xi_\perp, V)} \frac{\partial}{\partial V} \epsilon_{\text{LRA}}(\xi_\perp, V), \quad (5a)$$

$$\frac{\partial d_\parallel}{\partial V} = \frac{1}{\epsilon_m - \epsilon_d} \int_{-\infty}^{\infty} d\xi_\perp \frac{\partial}{\partial V} \epsilon_{\text{LRA}}(\xi_\perp, V). \quad (5b)$$

Here, ϵ_m and ϵ_d are the bulk permittivities of the metal and surrounding dielectric, respectively (for a detailed derivation see Supplementary Section 1.5). For both components, the integrands in equations (5a) and (5b) contain the partial derivative of the local permittivity with respect to the applied voltage $\partial_V \epsilon_{\text{LRA}}$. That is, they depend on the induced electron density $\Delta n_0(\xi_\perp, V)$, which can be related to the classical total induced

surface electron density $\Delta n_0(V)$ via the integral

$$\int_{-\infty}^{\infty} d\xi_{\perp} \Delta n_0(\xi_{\perp}, V) = \Delta n_0(V). \quad (6)$$

The voltage-induced surface electron density can be obtained from the discontinuity of the normal component of the static displacement field $D_{\perp} = \epsilon_0 \kappa E_{\perp}$, where E_{\perp} is the normal component of the static electric field (see Fig. 3b) in the dielectric and κ is the dielectric constant. Furthermore, we can express the induced surface electron density in terms of a surface capacitance C_s as $\Delta n_0(V) \simeq C_s V / q_e$, where q_e is the electron charge, showing explicitly the dependency on the applied voltage. This implies that we can represent the induced electron density as

$$\Delta n_0(\xi_{\perp}, V) \simeq p(\xi_{\perp}) \frac{C_s V}{q_e}, \quad (7)$$

where $p(\xi_{\perp})$ is the probability distribution of the induced electron density per unit length, which follows the shape of the induced electron density (see Fig. 1e) and satisfies the normalization condition $\int dx_{\perp} p(\xi_{\perp}) = 1$. In the case of the d_{\parallel} component, using equation (4) for the evaluation of equation (5b) reduces to the evaluation of the partial derivative with respect to voltage of the integral Eq. (6). This expression can be evaluated by employing equation (7), which implies that the perturbation is independent of the shape of the induced electron density and only depends on the amount of the induced charge. Therefore, the perturbation coefficient can be expressed analytically with a purely classical term

$$\frac{\partial d_{\parallel}(\mathbf{r}_s, V)}{\partial V} \simeq \frac{1}{\epsilon_d - \epsilon_m} \frac{\omega_p^2}{\omega^2 + i\gamma\omega} \frac{C_s(\mathbf{r}_s)}{q_e} \frac{1}{n_0}, \quad (8)$$

where the surface position dependency \mathbf{r}_s has been reintroduced through the surface capacitance $C_s(\mathbf{r}_s)$, arising from the uneven distribution of static charges. One can show that the perturbed d_{\parallel} parameter directly leads to a perturbed surface conductivity $\Delta\sigma_s \propto \Delta d_{\parallel}$, the same result as provided by the classical model of Bohren and Hunt (for a detailed discussion see Supplementary Section 1.6). In addition to the perturbation of the surface conductivity resulting from the bulk electrons, other, non-classical effects, such as conduction through surface-states, can also impact the d_{\parallel} perturbation coefficient [47, 48], especially since our resonators are fabricated from single crystalline gold microplatelets with Au(111) top and bottom surfaces [54, 55].

In the case of the d_{\perp} component, by inserting equation (7) for the induced electron density into equation (4), the surface position dependency carried by the surface capacitance can be brought outside the integral in equation (5a) which results in the following expression

$$\frac{\partial d_{\perp}(\mathbf{r}_s, V)}{\partial V} \simeq \frac{\epsilon_d \epsilon_m}{\epsilon_d - \epsilon_m} \frac{\omega_p^2}{\omega^2 + i\gamma\omega} \frac{C_s(\mathbf{r}_s)}{q_e} \frac{1}{n_0} \int_{-\infty}^{\infty} d\xi_{\perp} \frac{p(\xi_{\perp})}{\epsilon_{\text{LRA}}^2(\xi_{\perp})}. \quad (9)$$

Evaluation of the integral (9) is not trivial since it depends on the shape of the induced electron density and the local permittivity. For simplicity, we assume that the background permittivity (4) follows the distribution of the equilibrium electron density (see Fig. 3a), which is derived from DFT calculations using the jellium approximation. Subsequently, as one transitions from the metal to the dielectric, the equilibrium electron density smoothly changes from the bulk value to zero. This results in a position, $\xi_{\perp,0}$, where the local permittivity (real part) crosses zero. Therefore, accurately evaluating the integral in equation (9) necessitates a precise knowledge of the shape of the permittivity in the vicinity of $\xi_{\perp,0}$.

B. Simulations

To evaluate the perturbation coefficients (8) and (9), we need to evaluate the equilibrium $n_0(\xi_{\perp})$, and the induced electron density $\Delta n_0(\xi_{\perp}, V)$, as well as the position dependent surface capacitance $C_s(\mathbf{r}_s)$. To this end we perform DFT calculations for a thin slab of jellium (8 nm), and electrostatic simulations for the geometry under investigation (for more details refer to Supplementary Section 1.7-8). In Fig. 3d we show the spectrally dependent, interface averaged d -parameter perturbation coefficients for 140 nm long resonator. Real and imaginary parts for all the perturbation coefficients exhibit negative values and show gradual variations across the spectrum. These coefficients have magnitudes on the order of 0.1 pm/V. Therefore, for typical voltages of around 10 V, the resulting perturbations $\langle \Delta d \rangle = \langle \partial_V d \rangle V$ will be approximately 1 pm. Negative signs in the real parts are expected, since for a positive bias we deplete the surface from polarizable material, effectively reducing the size of the resonator. Although in Fig. 3d we show only the case of the gold-glass interface, the result is similar for the gold-air interface.

Next, we examine the extent to which each component of the d -parameters influences the scattering spectrum. First, numerical simulations are conducted to obtain the scattering resonance as shown in the inset of Fig. 3e. In the second step, we vary each of the d -parameters independently by 1 pm of surface-averaged value and calculate the relative change of scattering $\Delta S/S_0$ using mesoscopic boundary conditions (see Fig. 3e) [40, 49, 56]. We find that the calculated changes are of the same order of magnitude as the experimentally observed ones. Furthermore, we can see that for a real part perturbation of 1 pm in the $d_{\parallel}(d_{\perp})$ component (denoted as $\text{Re}_{\parallel}(\text{Re}_{\perp})$ in Fig. 2c, respectively) we obtain dispersive curves with maximal changes on the slopes of the resonance, and a zero-crossing point almost perfectly aligned with the position of the resonance frequency. These characteristic shapes of the relative changes are produced by a change in the resonance position (compare orange curves in Fig. 3d and Fig. 1e). Moreover, introducing a perturbation of 1 pm to the imaginary part of the $d_{\parallel}(d_{\perp})$ component (denoted as $\text{Im}_{\parallel}(\text{Im}_{\perp})$ in Fig. 2c) predominantly influences the width of the resonance (compare green curves in Fig. 3c and Fig. 1e). We can see that the induced changes in scattering for two parameters are of similar magnitude but act in the opposite directions while the perturbation coefficients have the same sign, implying a competing effects. This can explain why, in the quantum approach by Li

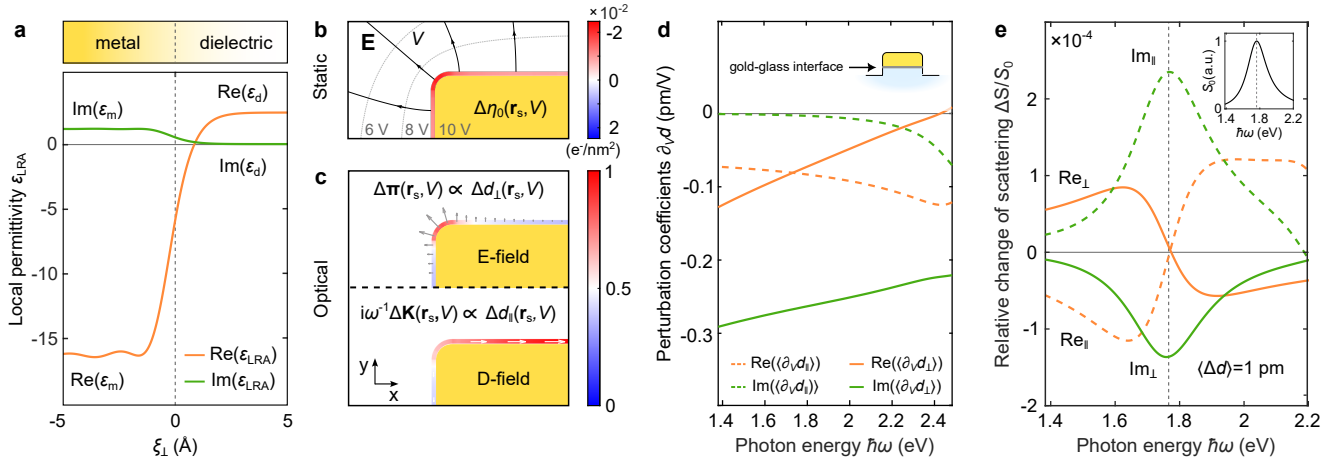


FIG. 3. **Influence of d -parameter perturbations on a plasmonic resonance.** **a**, Spatial dependency of local permittivity at the gold-glass interface. **b**, Simulated static electric field lines at half of the antenna height (black arrowed lines) and contours of electric potential (gray dashed lines) for a 10 V equipotential at the surface of the structure. Excess electrons are non-uniformly distributed across the surface, represented by the induced surface electron density $\Delta n_0(\mathbf{r}_s, V) = C_s(\mathbf{r}_s)V/q_e$ (surface color). **c**, Simulated perturbed surface polarization $\mathbf{P}_s(V)$ corresponding to an out-of-plane response (up) with electric field, and an in-plane response (down) with displacement field. **d**, Spectral dependency of surface averaged d -parameter perturbation coefficients for the gold-glass interface calculated with Eq. (8) and (9). The d_\perp component contributions are depicted with a solid lines, while the d_\parallel component are represented with dashed lines. Real parts are given in orange, and imaginary parts in green. **e**, Calculated relative change of scattering $\Delta S/S_0$ for 1 pm of introduced surface-averaged d -parameter perturbations. The inset shows the calculated unperturbed scattering spectrum S_0 .

and co-workers, with a strong out-of-plane response, it is expected to observe a strong red-shift and resonance broadening for a negatively charged resonator [29]. In contrast, the classical model proposed by Bohren and Hunt, solely influenced by an in-plane response, predicts a blue-shift.

C. Comparison of experiment and model

By summing all d -parameter contributions to the relative change of scattering, we can determine the total change in resonance and directly compare it to experimental data, as presented in Fig. 4. To ensure that simulations and experiments are treated on an equal footing, the unperturbed resonance position ω_{r0} and width γ_{r0} are obtained by fitting a Lorentzian line shape with a linear background to the scattering spectrum S_0 (see Supplementary Section 1.9). Fig. 4a shows that the simulated curve closely matches the shape of the measured resonance. Minor discrepancies in the peak position and resonance width can be attributed to inaccuracies in the model's geometry and the material data. In Fig. 4b, alongside the experimental data, we show the relative change of scattering obtained from simulations for 10 V of applied potential. We can see that the perturbation caused solely by the d_\parallel component, which is, as pointed out, a purely classical term, exhibits a similar spectral shape as the experimental result. This similarity is reflected in the obtained spectral shift $\hbar\Delta\omega_r$, which is determined to be $(-24.90 \pm 0.01) \mu\text{eV}$ in the simulations, whereas the measured value is $(-23 \pm 2) \mu\text{eV}$ – we have used one standard deviation to represent the uncertainties. There is, however, a significant difference to observe when examining the point at which the relative change in scattering crosses zero. In the experimental data, this spectral position is shifted

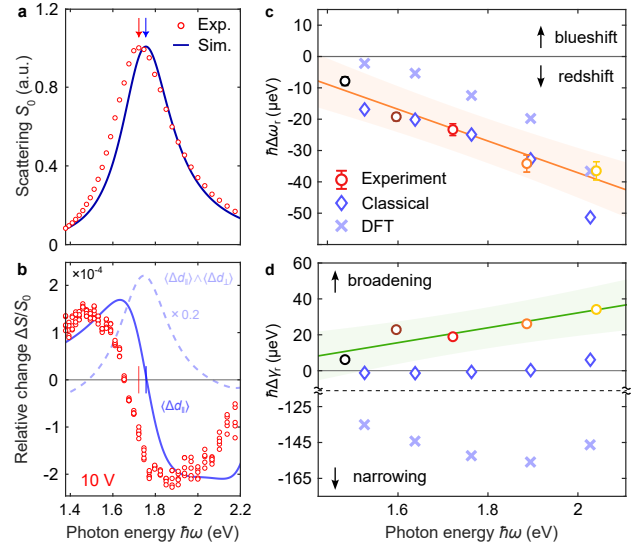


FIG. 4. **Comparison of experiment and model.** **a**, Scattering spectrum for 140 nm long resonator in experiment (red circles) and simulation (dark blue line). **b**, Relative change of scattering corresponding to resonances presented in **a** for a 10 V of voltage amplitude. Solid blue line corresponds to classical model while light-blue dashed line to model based on DFT. Small dashes represent the position of resonance frequency presented in **a**. **d,e**, Perturbations of resonant frequencies and resonance widths retrieved from experiments and simulations for both classical (blue diamonds) and DFT model (light blue crosses). Color code of the nanoresonators is identical to Fig. 2.

towards the blue compared to the resonance position, which suggests that the resonance has broadened (see Fig. 1c), with an increase in spectral width $\hbar\Delta\gamma_r = (19 \pm 1) \mu\text{eV}$. This feature is not accounted for by the classical model – the d_{\parallel} component perturbation has negligible imaginary part (see Fig. 2d), and therefore does not affect the loss of the system, as reflected in the obtained $\hbar\Delta\gamma_r$ value of $(0.7 \pm 0.1) \mu\text{eV}$. In contrast, when we include the d_{\perp} component perturbation obtained from the DFT calculations, which is dominated by the large imaginary part (see Fig. 3d), we observe a maximum relative change of approximately 1×10^{-3} at resonance. This implies a significant narrowing of the resonance for positive bias with a $\hbar\Delta\gamma_r$ value of $(-152.8 \pm 0.1) \mu\text{eV}$ and reduced spectral shift $\hbar\Delta\omega_r = (-12.4 \pm 0.4) \mu\text{eV}$. However, none of the d_{\perp} -component effects have been observed in the experiment. Furthermore, as shown in Fig. 4c,d, both the resonances red-shifting and broadening occur for the resonators of different lengths, with scattering spectra presented in Fig. 2b. We can see that the classical model predicts the spectral shift well, however cannot account for the spectral broadening. The non-classical model based on DFT, which includes both in-plane and out-of-plane responses, cannot account for either.

D. Discussion on the relative contributions

The absence of the d_{\perp} -component effects, as calculated from DFT, suggests that contributions from the d_{\perp} component are effectively suppressed in the experiment. Assuming that the DFT jellium calculations – at least qualitatively – captures the surface electrodynamic phenomena of the real physical surface, this leads to the conclusion that either nonlocal effects counteract the perturbation as calculated with the LRA, or there is an anisotropy of the perturbed local permittivity with suppressed out-of-plane response. If the out-of-plane motion is suppressed, one possible explanation for the narrowing of the resonance with added electrons is that added electrons preferentially occupy surface states and impact the d_{\parallel} perturbation coefficient as our resonators are fabricated from single crystalline gold microplatelets with Au(111) top and bottom surfaces. To further validate these assumptions, additional experiments are required that can clearly separate the contributions of the nanoresonator’s eigenfrequency change stemming from the perturbation of the d_{\parallel} and d_{\perp} component. Fig. 3e shows that the perturbation strengths for all components are non-negligible, which can be attributed to the simplicity of the chosen geometry that does not have any pronounced geometrical features and large field enhancements. One possible way to disentangle the contributions stemming from d_{\parallel} and d_{\perp} , is by using a dimer antenna with a narrow gap [57]. Such a structure exhibits a large field enhancement in the gap in both the static and optical regimes, which according to equation (2), should enhance contributions from the d_{\perp} component. Nevertheless, due to anti-symmetric static perturbation, one should choose antenna with an asymmetric gap [29, 53].

V. Conclusion

We have presented both theoretical and experimental investigation of charged plasmonic resonators and their optical response. In our experimental work, we have shown that direct electrical charging leads to a resonance shift and a change in the line width. Under the influence of a positive bias, the resonance shifts towards longer wavelengths while simultaneously increasing in width while the opposite effects occur under a negative bias. To explain the experimental observations, we place the charging effects within the general framework of surface-response functions taking into account both in-plane and out-of-plane responses. Feibelman d -parameter perturbations are calculated from a basic model derived from the equilibrium and induced electron densities at a charged jellium-air interface within LRA. We have derived an analytical expression of the d_{\parallel} component perturbation and demonstrated that it exhibits a purely classical behavior, which is equivalent to a perturbation of the surface conductivity defined with bulk parameters. Moreover, the perturbed in-plane response accounts for the observed spectral shift of the resonance frequency observed in experiments. However, the intriguing spectral narrowing of the resonance as more electrons are added to the resonator cannot be explained by our basic model. We attribute these discrepancy to unaccounted non-classical effects such as: nonlocality and anisotropy of the local permittivity. To provide stronger evidence for these claims, further modeling efforts that go beyond jellium considerations are required. Moreover, as discussed in the text, exploring optimized geometries with stronger field localization will aid to more effectively distinguish the contribution arising from the d_{\perp} component. Additionally, we observed that smaller resonators exhibit more pronounced alterations in resonance behavior, because of their increased surface-to-volume ratio. If these resonators are further downsized, this effect is anticipated to become even more prominent, offering potential for the development of electrically-driven ultra-fast optical modulators by gaining control over non-classical surface effects.

Methods

Numerical simulations. The perturbation of the optical response of a plasmonic nanoresonator under electrostatic biasing is numerically determined using the commercially available FEM solver (COMSOL Multiphysics 6.0) [58] for the electrodynamics. Our simulations involve a two-step process. Initially, we solve for the electrostatic field by applying a potential V to the structure using the AC/DC Module. This step allows us to obtain the induced surface electron density $\Delta\eta_0(\mathbf{r}_s, V)$. The ground potential is placed infinitely far away by employing an infinite element domain layer. In the second step, we conduct optical simulations using the wave optics module to analyze the scattering cross Section based on the local perturbation in the d -parameters influenced by the induced surface electron density. To introduce perturbations in the d -parameters, we employ mesoscopic boundary condi-

tions (see Supplementary Section 1.6) implemented with an auxiliary potential method, as described in Ref. 40. The structure is excited with a plane wave polarized along the long axis of the nanoresonator, and the scattered light is collected at the bottom hemisphere to mimic the experimental setup. The optical permittivity of gold is taken from the experimental values for mono-crystalline gold provided by Olmon *et al.* [59], while glass is modeled using Sellmeier coefficients. For more information, please refer to Supplementary Section 1.3.

Sample fabrication. Mono-crystalline gold microplatelets, measuring 50 nm in thickness, are synthesized through a wet-chemical process outlined in Ref. 52. These microplatelets are then transferred onto a glass coverslip (24 mm \times 24 mm #1.5 Menzel) with evaporated metal layers featuring an array of electrode pads prepared by optical lithography and electron beam physical vapor deposition (20 nm chromium adhesion layer, 80 nm gold layer). The microplatelets are carefully positioned over the glass window on structured microscopic electrodes, ensuring a conductive connection between the flake and the metal film. Nanoresonator fabrication is conducted as described in Ref. 53.

Optical characterization. To capture dark-field scattering spectra of plasmonic nanoresonators, we employ an inverted optical microscope (TE2000-U, Nikon) equipped with a nanopositioning piezostage (NanoLPS200, Mad City Labs Inc.) and an oil-immersion microscope objective (PlanApochromat, 100 \times , NA = 1.45, Nikon). As excitation source, we utilize a supercontinuum laser (SuperK FIANIUM, FIR-20, NKT) that is spectrally shaped and scanned in 10 nm increments from 500 nm to 900 nm using an acousto-optic tunable filter (SuperK SELECT, NKT). The light from the laser is sent through a 300 μ m pinhole and focused to the back focal plane of the oil-immersion microscope objective via a 500 mm lens, providing a collimated beam at the sample. To separate the detection and excitation beam paths, a 50:50 beam splitter is employed. Light scattered by the structure above the critical angle and light reflected directly from the sample are separated using a circular beam block. Additionally, to minimize potential stray light, an iris is positioned in the intermediate image plane and adjusted until the background is completely suppressed. The signal is collected using an optical power meter (1835-C, Newport). See also Supplementary Section 2.1-2.3.

Electro-optical measurements. The nanoresonators are electrically connected to the macroscopic electrode pads using thin connector lines. They are then further connected via micro-manipulators to a function generator (DS 345, Stanford Research Instruments). An AC voltage is applied to the structure, and the scattered light, guided to the detector, is divided into two collecting channels using a 90:10 beam splitter. The majority of the light is captured by a silicon photodetector (DET36A2, Thorlabs) with a rise time of 14 ns, while the remaining portion is detected using an optical power meter (1835-C, Newport). The electrical signal from the photode-

tor is directed to a lock-in amplifier (DSP 7260, EG&G), with the reference signal obtained directly from the function generator output using a T-splitter. To enable the recording of correlated data, the entire process is monitored via a LabVIEW program. Throughout the measurements, the sample is continuously blow-dried using a laminar nitrogen stream.

Acknowledgments. T. F. acknowledges funding by the Volkswagen Foundation via an ‘Experiment!’ grant (95869), by the Marie Skłodowska-Curie Actions (MSCA) individual fellowship project PoSHGOAT (project- id 837928) and participation in CA19140 (FIT4NANO), supported by COST (European Cooperation in Science and Technology). B. H. gratefully acknowledges funding by the Deutsche Forschungsgemeinschaft (DFG, German Research Foundation) under Germany’s Excellence Strategy through the Würzburg-Dresden Cluster of Excellence on Complexity and Topology in Quantum Matter ct.qmat (EXC 2147, Project ID ST0462019) as well as through a regular project (HE5618/10-1) and a Reinhard Koselleck project (HE5618/6-1). The Volkswagen foundation is acknowledged for funding via research grant 93437-1. N. A. M. is a VILLUM Investigator supported by VILLUM FONDEN (Grant No. 16498). The Center for Polariton-driven Light–Matter Interactions (POLIMA) is funded by the Danish National Research Foundation (Project No. DNRF165).

Author contributions L. Z. conceived the idea and designed the experiment. J. M. fabricated the structures and performed the SEM measurements. R. K. and L. Z. built and optimized the electro-optical setup. L. Z. performed the electro-optical experiments. N. A. M. provided the derivation of the d -parameter perturbations. C. W. performed the DFT calculations. L. Z. conducted the FEM simulations. L. Z. analyzed the data and drafted the manuscript with input from all the authors. B. H. and T. F. supervised the project.

Data and code is available upon request to L. Z. and T. F.

Correspondence should be addressed to L. Z. and T. F.

- [1] R. H. Ritchie. Plasma losses by fast electrons in thin films. *Physical Review*, 106(5):874, 1957.
- [2] P. Muhlschlegel, H.-J. Eisler, O. J. F. Martin, B. Hecht, and D. W. Pohl. Resonant optical antennas. *Science*, 308(5728):1607–1609, 2005.
- [3] L. Novotny. Effective wavelength scaling for optical antennas. *Physical Review Letters*, 98(26):266802, 2007.
- [4] A. G. Curto, G. Volpe, T. H. Taminiau, M. P. Kreuzer, R. Quidant, and N. F. van Hulst. Unidirectional emission of a quantum dot coupled to a nanoantenna. *Science*, 329(5994):930–933, 2010.
- [5] M. W. Knight, H. Sobhani, P. Nordlander, and N. J. Halas. Photodetection with active optical antennas. *Science*, 332(6030):702–704, 2011.
- [6] R. Zhang, Y. Zhang, Z. C. Dong, S. Jiang, C. Zhang, L. G. Chen, L. Zhang, Y. Liao, J. Aizpurua, Y. Luo, J. L. Yang, and J. G. Hou. Chemical mapping of a single molecule by plasmon-enhanced Raman scattering. *Nature*, 498(7452):82–86, 2013.
- [7] J. Kern, R. Kullock, J. Prangma, M. Emmerling, M. Kamp, and B. Hecht. Electrically driven optical antennas. *Nature Photonics*, 9(9):582–586, 2015.
- [8] M. Celebrano, X. Wu, M. Baselli, S. Großmann, P. Biagioni, A. Locatelli, C. De Angelis, G. Cerullo, R. Osellame, B. Hecht, et al. Mode matching in multiresonant plasmonic nanoantennas for enhanced second harmonic generation. *Nature Nanotechnology*, 10(5):412–417, 2015.
- [9] R. Chikkaraddy, B. de Nijs, F. Benz, S. J. Barrow, O. A. Scherman, E. Rosta, A. Demetriadou, P. Fox, O. Hess, and J. J. Baumberg. Single-molecule strong coupling at room temperature in plasmonic nanocavities. *Nature*, 535(7610):127–130, 2016.
- [10] N. Jiang, X. Zhuo, and J. Wang. Active plasmonics: principles, structures, and applications. *Chemical Reviews*, 118(6):3054–3099, 2017.
- [11] F. Wang, Y. Zhang, C. Tian, C. Girit, A. Zettl, M. Crommie, and Y. R. Shen. Gate-variable optical transitions in graphene. *Science*, 320(5873):206–209, 2008.
- [12] F. Bonaccorso, Z. Sun, T. Hasan, and A. C. Ferrari. Graphene photonics and optoelectronics. *Nature Photonics*, 4(9):611–622, 2010.
- [13] M. Liu, X. Yin, E. Ulin-Avila, B. Geng, T. Zentgraf, L. Ju, F. Wang, and X. Zhang. A graphene-based broadband optical modulator. *Nature*, 474(7349):64–67, 2011.
- [14] BG McMillan, LEA Berlouis, FR Cruickshank, and PF Brevet. Reflectance and electrolyte electroreflectance from gold nanorod arrays embedded in a porous alumina matrix. *Journal of Electroanalytical Chemistry*, 599(2):177–182, 2007.
- [15] P. Mulvaney, J. Pérez-Juste, M. Giersig, L. M. Liz-Marzán, and C. Pecharrmán. Drastic surface plasmon mode shifts in gold nanorods due to electron charging. *Plasmonics*, 1:61–66, 2006.
- [16] C. Novo, A. M. Funston, A. K. Gooding, and P. Mulvaney. Electrochemical charging of single gold nanorods. *Journal of the American Chemical Society*, 131(41):14664–14666, 2009.
- [17] T. Miyazaki, R. Hasegawa, H. Yamaguchi, H. Oh-oka, H. Nagato, I. Amemiya, and S. Uchikoga. Electrical control of plasmon resonance of gold nanoparticles using electrochemical oxidation. *The Journal of Physical Chemistry C*, 113(19):8484–8490, 2009.
- [18] SK Dondapati, M Ludemann, R Muller, S Schwieger, A Schwemer, B Handel, D Kwiatkowski, M Djiango, E Runge, and TA Klar. Voltage-induced adsorbate damping of single gold nanorod plasmons in aqueous solution. *Nano letters*, 12(3):1247–1252, 2012.
- [19] T. A. Petach, M. Lee, R. C. Davis, A. Mehta, and D. Goldhaber-Gordon. Mechanism for the large conductance modulation in electrolyte-gated thin gold films. *Physical Review B*, 90(8):081108, 2014.
- [20] Chad P Byers, Benjamin S Hoener, Wei-Shun Chang, Mustafa Yorulmaz, Stephan Link, and Christy F Landes. Single-particle spectroscopy reveals heterogeneity in electrochemical tuning of the localized surface plasmon. *The Journal of Physical Chemistry B*, 118(49):14047–14055, 2014.
- [21] Ana M Brown, Matthew T Sheldon, and Harry A Atwater. Electrochemical tuning of the dielectric function of au nanoparticles. *ACS Photonics*, 2(4):459–464, 2015.
- [22] S. S. E. Collins, X. Wei, T. G. McKenzie, A. Funston, and P. C. Mulvaney. Single gold nanorod charge modulation in an ion gel device. *Nano Letters*, 16(11):6863–6869, 2016.
- [23] B. S. Hoener, H. Zhang, T. S. Heiderscheidt, S. R. Kirchner, A. S. De Silva Indrasekara, R. Baiyasi, Y. Cai, P. Nordlander, S. Link, C. F. Landes, and W.-S. Chang. Spectral response of plasmonic gold nanoparticles to capacitive charging: morphology effects. *The Journal of Physical Chemistry Letters*, 8(12):2681–2688, 2017.
- [24] T. Liu, M. Li, Y. Wang, Y. Fang, and W. Wang. Electrochemical impedance spectroscopy of single Au nanorods. *Chemical Science*, 9(19):4424–4429, 2018.
- [25] R. A. Maniyara, D. Rodrigo, R. Yu, J. Canet-Ferrer, D. S. Ghosh, R. Yongsunthon, D. E. Baker, A. Rezikyan, F. J. García de Abajo, and V. Pruneri. Tunable plasmons in ultrathin metal films. *Nature Photonics*, 13(5):328–333, 2019.
- [26] M. T. Sheldon, J. van de Groep, A. M. Brown, A. Polman, and H. A. Atwater. Plasmoelectric potentials in metal nanostructures. *Science*, 346(6211):828–831, 2014.
- [27] C. F. Bohren and A. J. Hunt. Scattering of electromagnetic waves by a charged sphere. *Canadian Journal of Physics*, 55(21):1930–1935, 1977.
- [28] M. Zapata Herrera, J. Aizpurua, A. K. Kazansky, and A. G. Borisov. Plasmon response and electron dynamics in charged metallic nanoparticles. *Langmuir*, 32(11):2829–2840, 2016.
- [29] W. Li, Q. Zhou, P. Zhang, and X.-W. Chen. Direct electro plasmonic and optic modulation via a nanoscopic electron reservoir. *Physical Review Letters*, 128(21):217401, 2022.
- [30] P. J. Feibelman. Surface electromagnetic fields. *Progress in Surface Science*, 12(4):287–407, 1982.
- [31] U. Kreibig and L. Genzel. Optical absorption of small metallic particles. *Surface Science*, 156:678–700, 1985.
- [32] J. Tiggesbäumker, L. Köller, K.-H. Meiwes-Broer, and A. Liebsch. Blue shift of the mie plasma frequency in Ag clusters and particles. *Physical Review A*, 48(3):R1749, 1993.
- [33] E. Cottancin, G. Celep, J. Lermé, M. Pellarin, J. R. Huntzinger, J. L. Vialle, and M. Broyer. Optical properties of noble metal clusters as a function of the size: comparison between experiments and a semi-quantal theory. *Theoretical Chemistry Accounts*, 116(4-5):514–523, 2006.
- [34] J. Zuloaga, E. Prodan, and P. Nordlander. Quantum description of the plasmon resonances of a nanoparticle dimer. *Nano Letters*, 9(2):887–891, 2009.
- [35] K. J. Savage, M. M. Hawkeye, R. Esteban, A. G. Borisov, J. Aizpurua, and J. J. Baumberg. Revealing the quantum regime in tunnelling plasmonics. *Nature*, 491(7425):574–577, 2012.
- [36] J. A. Scholl, A. L. Koh, and J. A. Dionne. Quantum plas-

- mon resonances of individual metallic nanoparticles. *Nature*, 483(7390):421–427, 2012.
- [37] C. Ciraci, R. T. Hill, J. J. Mock, Y. Urzhumov, A. I. Fernández-Domínguez, S. A. Maier, J. B. Pendry, A. Chilkoti, and D. R. Smith. Probing the ultimate limits of plasmonic enhancement. *Science*, 337(6098):1072–1074, 2012.
- [38] S. Raza, N. Stenger, S. Kadkhodazadeh, S. V. Fischer, N. Kostesha, A.-P. Jauho, A. Burrows, M. Wubs, and N. A. Mortensen. Blueshift of the surface plasmon resonance in silver nanoparticles studied with EELS. *Nanophotonics*, 2(2):131–138, 2013.
- [39] W. Zhu, R. Esteban, A. G. Borisov, J. J. Baumberg, P. Nordlander, H. J. Lezec, J. Aizpurua, and K. B. Crozier. Quantum mechanical effects in plasmonic structures with subnanometre gaps. *Nature Communications*, 7:11495, 2016.
- [40] Y. Yang, D. Zhu, W. Yan, A. Agarwal, M. Zheng, J. D. Joannopoulos, P. Lalanne, T. Christensen, K. K. Berggren, and M. Soljačić. A general theoretical and experimental framework for nanoscale electromagnetism. *Nature*, 576(7786):248–252, 2019.
- [41] S. Boroviks, Z.-H. Lin, V. A. Zenin, M. Ziegler, A. Dellith, P. A. D. Gonçalves, C. Wolff, S. I. Bozhevolnyi, J.-S. Huang, and N. A. Mortensen. Extremely confined gap plasmon modes: when nonlocality matters. *Nature Communications*, 13:3105, 2022.
- [42] N. A. Mortensen, P. A. D. Gonçalves, F. A. Shuklin, J. D. Cox, C. Tserkezis, M. Ichikawa, and C. Wolff. Surface-response functions obtained from equilibrium electron-density profiles. *Nanophotonics*, 10(14):3647–3657, 2021.
- [43] S. Raza, S. I. Bozhevolnyi, M. Wubs, and N. A. Mortensen. Nonlocal optical response in metallic nanostructures. *Journal of Physics: Condensed Matter*, 27(18):183204, 2015.
- [44] D. Jin, Q. Hu, D. Neuhauser, F. von Cube, Y. Yang, R. Sachan, T. S. Luk, D. C. Bell, and N. X. Fang. Quantum-spillover-enhanced surface-plasmonic absorption at the interface of silver and high-index dielectrics. *Physical Review Letters*, 115(19):193901, 2015.
- [45] J. B. Khurgin. Ultimate limit of field confinement by surface plasmon polaritons. *Faraday discussions*, 178:109–122, 2015.
- [46] T. V. Shahbazyan. Landau damping of surface plasmons in metal nanostructures. *Physical Review B*, 94(23):235431, 2016.
- [47] N. A. Mortensen. Mesoscopic electrodynamics at metal surfaces. *Nanophotonics*, 10(10):2563–2616, 2021.
- [48] A. Rodríguez Echarri, P. A. D. Gonçalves, C. Tserkezis, F. J. García de Abajo, N. A. Mortensen, and J. D. Cox. Optical response of noble metal nanostructures: quantum surface effects in crystallographic facets. *Optica*, 8(5):710–721, 2021.
- [49] T. Christensen, W. Yan, A.-P. Jauho, M. Soljačić, and N. A. Mortensen. Quantum corrections in nanoplasmonics: shape, scale, and material. *Physical Review Letters*, 118(15):157402, 2017.
- [50] P. Lalanne, W. Yan, K. Vynck, C. Sauvan, and J.-P. Hugonin. Light interaction with photonic and plasmonic resonances. *Laser & Photonics Reviews*, 12(5):1700113, 2018.
- [51] J. Yang, H. Giessen, and P. Lalanne. Simple analytical expression for the peak-frequency shifts of plasmonic resonances for sensing. *Nano Letters*, 15(5):3439–3444, 2015.
- [52] E. Krauss, R. Kulloock, X. Wu, P. Geisler, N. Lundt, M. Kamp, and B. Hecht. Controlled growth of high-aspect-ratio single-crystalline gold platelets. *Crystal Growth & Design*, 18(3):1297–1302, 2018.
- [53] Jessica Meier, Luka Zurak, Andrea Locatelli, Thorsten Feichtner, René Kulloock, and Bert Hecht. Controlling field asymmetry in nanoscale gaps for second harmonic generation. *Advanced Optical Materials*, page 2300731, 2022.
- [54] Binghai Yan, Benjamin Stadtmüller, Norman Haag, Sebastian Jakobs, Johannes Seidel, Dominik Jungkenn, Stefan Mathias, Mirko Cinchetti, Martin Aeschlimann, and Claudia Felser. Topological states on the gold surface. *Nature communications*, 6(1):10167, 2015.
- [55] Pascal Dreher, David Janoschka, Bettina Frank, Harald Giessen, and Frank-J Meyer zu Heringdorf. Focused surface plasmon polaritons coherently couple to electronic states in above-threshold electron emission. *Communications Physics*, 6(1):15, 2023.
- [56] W. Yan, M. Wubs, and N. A. Mortensen. Projected dipole model for quantum plasmonics. *Physical Review Letters*, 115(13):137403, 2015.
- [57] J. C. Prangma, J. Kern, A. G. Knapp, S. Grossmann, M. Emmerling, M. Kamp, and B. Hecht. Electrically connected resonant optical antennas. *Nano Letters*, 12(8):3915–3919, 2012.
- [58] COMSOL Multiphysics v. 6.0. www.comsol.com. COMSOL AB, Stockholm, Sweden.
- [59] R. L. Olmon, B. Slovick, T. W. Johnson, D. Shelton, S.-H. Oh, G. D. Boreman, and M. B. Raschke. Optical dielectric function of gold. *Physical Review B*, 86(23):235147, 2012.

Supplementary material

Direct electrical modulation of surface response in a single plasmonic nanoresonator

Luka Zurak¹, Christian Wolff², Jessica Meier¹, René Kullock¹, N. Asger Mortensen^{2,3}, Bert Hecht¹, and Thorsten Feichtner¹

¹Nano-Optics and Biophotonics Group, Experimental Physics 5, Institute of Physics, University of Würzburg, Germany

²POLIMA - Center for Polariton-driven Light-Matter Interactions, University of Southern Denmark, Campusvej 55, DK-5230 Odense M, Denmark

³Danish Institute for Advanced Study, University of Southern Denmark, Campusvej 55, DK-5230 Odense M, Denmark

Contents

13	1 Model	2
14	1.1 Classical models	2
15	1.2 Feibelman d -parameters	3
16	1.3 Mesoscopic boundary conditions	3
17	1.4 Lossy harmonic oscillator	3
18	1.5 Electron spill-out and LRA	4
19	1.6 Surface-response functions and classical surface model	5
20	1.7 Evaluating the d -parameters	5
21	1.8 Nanoresonator on a substrate	6
22	1.9 Effect of the d -parameters on the properties of plasmonic resonance	8
23	2 Experiment	10
24	2.1 Electro-optical setup	10
25	2.2 Scattering measurements	10
26	2.3 Characteristics of the excitation source	11
27	2.4 Exemplary lock-in measurements	12

1 Model

1.1 Classical models

When discussing the optical response of charged plasmonic nanoresonators, two classical models are relevant. These models assume that the excess charge arises from a variation in the number of free electrons N_0 .

Bulk model

In a simplified yet illustrative scenario, an excess charge is uniformly distributed throughout the volume V of the resonator – one should note that this assumption is obviously incorrect and misleading. Despite its flaws, this model is quite commonly employed to provide a rough estimate of the magnitude of the induced change. Consequently, this distribution induces changes in the material properties of the resonator by altering its bulk conductivity. The conductivity is given with the equation [1]:

$$\sigma_b = i\varepsilon_0 \frac{\omega_p^2}{\omega + i\gamma}, \quad (\text{S1.1})$$

where $\omega_p \propto \sqrt{n_0}$ is the plasma frequency and $n_0 = N_0/V$ is the free electron density. It can be shown that the resonance frequency of the system is proportional to the plasma frequency of the system. Therefore, changing the density of the free electrons effectively causes a change in the resonance frequency.

Surface model

Bohren and Hunt introduced the surface current model [2]. In this model, the excess charge induces a change in the surface electron density η_0 , resulting in a modification of the surface conductivity σ_s . By applying the Drude model to the thin surface charge layer consisting of electrons with mass m and charge q_e , the surface conductivity can be expressed using the following equation:

$$\sigma_s = i \frac{q_e^2}{m} \frac{\eta_0}{\omega + i\gamma}, \quad (\text{S1.2})$$

where γ is the collision rate at the surface. When the surface conductivity is perturbed, it induces a modification in the surface current $\mathbf{K} = \sigma_s \mathbf{E}_{\parallel}$, where \mathbf{E}_{\parallel} is the tangential component of the electric field at the surface. To incorporate the presence of the surface current in Maxwell's equations, the boundary condition for the tangential component of the magnetic field \mathbf{H} needs to be redefined as

$$\Delta \mathbf{H}_{\parallel} = \mathbf{K} \times \hat{x}_{\perp}, \quad (\text{S1.3})$$

where \hat{x}_{\perp} is normal unit vector pointing away from material 1 to material 2 and $\Delta \mathbf{H} = (\mathbf{H}_2 - \mathbf{H}_1)$. The implications of the surface model, regarding its influence on the resonance, are not as clear as those in the case of the bulk model. However, a direct comparison can be made when discussing the special case of a sphere [2]. For very small spheres compared to the wavelength of light in the surrounding medium ($r \ll \lambda$), only relevant coefficient in the Mie theory expansion is the first one. Therefore, one can express extinction cross section as

$$\sigma_{\text{ext}} = 4kr \text{Im} \left[\frac{\varepsilon_{\text{eff}} - 1}{\varepsilon_{\text{eff}} + 2} \right] \quad (\text{S1.4})$$

where ε_{eff} is effective relative permittivity of the particle, with resonance condition reached for frequency where $\text{Re}(\varepsilon_{\text{eff}}) = -2$. Effective relative permittivity is given as a sum of bulk and surface terms

$$\varepsilon_{\text{eff}} = \varepsilon_b - i \frac{\sigma_b + 2\sigma_s/r}{\omega}, \quad (\text{S1.5})$$

here ε_b stands for background permittivity due to interband transitions. This equation implies that the surface conductivity contributes to the bulk conductivity as $2\sigma_s/r$, or in other words, relative change of the resonance is now proportional to the relative change of the effective plasma frequency, containing the surface term

$$\omega_{\text{peff}} \propto \left(n_0 + 2 \frac{\eta_0}{r} \right)^{1/2}. \quad (\text{S1.6})$$

Therefore, for very small systems the surface model should provide similar result as the bulk, leading to the perturbation of the resonant frequency.

62 1.2 Feibelman d -parameters

63 In classical electrodynamics, an interface between a metal and a dielectric is considered to be infinitesi-
64 mally thin, suggesting that the induced charge density $\rho(\xi_\perp)$ is strictly confined to the interface, meaning
65 $\rho(\xi_\perp) \propto \delta(\xi_\perp)$ [3], where $\delta(\xi_\perp)$ is a delta function. However, in his seminal work [4] Feibelman demonstrated
66 that the first-order correction to the multipole expansion of induced charge density introduces two additional
67 quantities known as "d-parameters". The d -parameters, denoted as $d_\perp \equiv d_\perp(\omega)$ and $d_\parallel \equiv d_\parallel(\omega)$, are frequency-
68 dependent centroids of the induced charge density, and of the normal derivative of the tangential current $\mathbf{J}_\parallel(\xi_\perp)$,
69 respectively (see [3]). That is, we can express them with the following equations

$$d_\perp = \frac{\int_{-\infty}^{\infty} \xi_\perp \rho(\xi_\perp) d\xi_\perp}{\int_{-\infty}^{\infty} \rho(\xi_\perp) d\xi_\perp},$$

$$d_\parallel = \frac{\int_{-\infty}^{\infty} \xi_\perp \frac{\partial}{\partial \xi_\perp} J_\parallel(\xi_\perp) d\xi_\perp}{\int_{-\infty}^{\infty} \frac{\partial}{\partial \xi_\perp} J_\parallel(\xi_\perp) d\xi_\perp}. \quad (\text{S1.7})$$

70 The d -parameters serve as descriptors of the optical properties of realistic metal-dielectric interfaces, similar
71 to how permittivity characterizes the bulk properties. They provide information about the non-locality and
72 inhomogeneous nature of the medium in proximity of the interface. Consequently, they are an appropriate tool
73 for investigating the impact of electrostatically induced surface charge on the optical properties of plasmonic
74 nanoresonators.

75 Typically, the d -parameters are obtained through ab-initio calculations that examine the response of metal
76 surfaces to time-varying electric fields. For example, time-dependent density-functional theory (TDDFT) is
77 commonly employed for this purpose [5, 6]. In certain cases, analytical evaluations of the response can be per-
78 formed, such as through semiclassical hydrodynamic models [7, 8, 9]. However, in all instances, the approach to
79 retrieve the d -parameters has been to assess the non-equilibrium electron response and employ equation (S1.7).

80 1.3 Mesoscopic boundary conditions

81 As exemplified by Yang, Zhu and others [10], the d -parameters can be introduced into classical equations by
82 means of boundary conditions, as they govern the surface polarization given with equation (1) in the main
83 text. When incorporating this additional surface polarization at the interface between two materials, the revised
84 boundary conditions are as follows:

$$\Delta D_\perp = -i\omega^{-1} \nabla_\parallel \cdot \mathbf{K} = -d_\perp \nabla_\parallel E_\perp \quad (\text{S1.8a})$$

$$\Delta B_\perp = 0 \quad (\text{S1.8b})$$

$$\Delta \mathbf{E}_\parallel = -\frac{1}{\epsilon_0} \nabla_\parallel \pi = -d_\perp \nabla_\parallel E_\perp \quad (\text{S1.8c})$$

$$\Delta \mathbf{H}_\parallel = \mathbf{K} \times \mathbf{n} = i\omega d_\parallel \Delta \mathbf{D}_\parallel \times \mathbf{n} \quad (\text{S1.8d})$$

85 Boundary conditions are implemented in FEM simulations using the auxiliary field method as discussed in
86 Ref. [10].

87 1.4 Lossy harmonic oscillator

88 In classical terms, a lossy harmonic oscillator's resonance line shape can be described by a Lorentzian function
89 $L(\omega; \omega_r, \gamma_r)$ with resonance position ω_r and width γ_r (see Fig. 1d in the main text). It is straightforward to show
90 that a small perturbation of the resonance frequency $\Delta\omega_r$, produces a distinct line shape of the relative change
91 of resonance as shown in Fig. 1e in the main text. This can be expressed analytically as

$$\frac{\Delta L_{\omega_r}}{L_0} \simeq \frac{1}{L_0} \frac{\partial L}{\partial \omega_r} \Delta\omega_r = 2L_0(\omega - \omega_{r0})\Delta\omega_r, \quad (\text{S1.9})$$

92 where $\Delta L_{\omega_r} \equiv L(\omega; \omega_{r0} + \Delta\omega_r, \gamma_{r0}) - L(\omega; \omega_{r0}, \gamma_{r0})$ and $L_0 \equiv L(\omega; \omega_{r0}, \gamma_{r0})$ is the unperturbed resonance,
93 with resonance position ω_{r0} and width γ_{r0} . Extrema of the relative change curve are reached at frequencies

94 $\omega_{\pm} = \omega_{r0} \pm \gamma_{r0}/2$, where the relative change of the resonance is

$$\frac{\Delta L_{\omega_r}}{L_0} \Big|_{\omega=\omega_{\pm}} = \pm 2Q \frac{\Delta\omega_r}{\omega_{r0}}. \quad (\text{S1.10})$$

95 Here, $Q = \omega_r/\gamma_r$ stands for the quality factor of the resonance. In the case of a blue-shifted resonance ($\Delta\omega_r > 0$),
 96 the relative change reaches its maximum on the blue side of the resonance and a minimum on the red side (see
 97 Fig. 1b in the main text). Conversely, for a red-shifted resonance ($\Delta\omega_r < 0$), we expect to observe the opposite
 98 pattern. Additionally, the change in the resonance position can be determined by examining the slope of the
 99 relative change curve at the resonance frequency (see Fig. 1b in the main text):

$$\frac{\partial}{\partial\omega} \frac{\Delta L_{\omega_r}}{L_0} \Big|_{\omega=\omega_{r0}} = \frac{8Q}{\gamma_{r0}} \frac{\Delta\omega_r}{\omega_{r0}}. \quad (\text{S1.11})$$

100 A small perturbation of the resonance width $\Delta\gamma_r$, will also lead to a characteristic line shape of the relative
 101 change curve, given by the expression:

$$\frac{\Delta L_{\gamma_r}}{L_0} \simeq \frac{1}{L_0} \frac{\partial L}{\partial\gamma_r} \Delta\gamma_r = -L_0 \frac{\gamma_{r0}}{2} \Delta\gamma_r, \quad (\text{S1.12})$$

102 where $\Delta L_{\gamma_r} \equiv L(\omega; \omega_{r0}, \gamma_{r0} + \Delta\gamma_r) - L(\omega; \omega_{r0}, \gamma_{r0})$. Thus, the relative change of line shape follows the shape of
 103 the resonance, and an extremum is reached at the resonance frequency ω_{r0} , with a value of:

$$\frac{\Delta L_{\gamma_r}}{L_0} \Big|_{\omega=\omega_{r0}} = -2 \frac{\Delta\gamma_r}{\gamma_{r0}}, \quad (\text{S1.13})$$

104 where an increase/decrease in damping leads to an increase/decrease in resonance width and therefore to a
 105 negative/positive relative change.

106 1.5 Electron spill-out and LRA

107 A recent study [11] has revealed that even when considering the spill-out effect and employing the local-
 108 response approximation, there remains a finite contribution to the metallic surface-response functions. The
 109 contribution arising from spill-out effects can be obtained by considering the equilibrium electron density,
 110 assuming a smooth transition from its bulk value deep within the metal to zero outside. Calculating these
 111 contributions involves evaluating the following expressions

$$d_{\perp} = \frac{1}{\varepsilon_m^{-1} - \varepsilon_d^{-1}} \int_{-\infty}^{\infty} d\xi_{\perp} [\varepsilon_{\text{LRA}}^{-1}(\xi_{\perp}) - \varepsilon_{\text{PCA}}^{-1}(\xi_{\perp})], \quad (\text{S1.14a})$$

$$d_{\parallel} = \frac{1}{\varepsilon_m - \varepsilon_d} \int_{-\infty}^{\infty} d\xi_{\perp} [\varepsilon_{\text{LRA}}(\xi_{\perp}) - \varepsilon_{\text{PCA}}(\xi_{\perp})], \quad (\text{S1.14b})$$

112 which incorporate the dielectric function of the surrounding materials $\varepsilon_m, \varepsilon_d$ and its profile near the interface.
 113 Here, $\varepsilon_{\text{LRA}}(\xi_{\perp})$ is smoothly varying dielectric function governed by the electron spill-out (as described with
 114 equation (4) in the main text), while $\varepsilon_{\text{PCA}}(\xi_{\perp})$ is a piecewise-constant dielectric function. Since the dielectric
 115 function in the local-response approximation depends on the equilibrium electron density, for an applied voltage
 116 V the electron density will be perturbed at the interface with the surrounding dielectric material, resulting in a
 117 new equilibrium electron density $n_0(\xi_{\perp}, V) = n_0(\xi_{\perp}) + \Delta n_0(\xi_{\perp}, V)$. Consequently, this leads to the perturbation
 118 of the local dielectric function $\varepsilon_{\text{LRA}}(\xi_{\perp}, V) = \varepsilon_{\text{LRA}}(\xi_{\perp}) + \Delta\varepsilon_{\text{LRA}}(\xi_{\perp}, V)$. To inspect the influence of the applied
 119 voltage on the d -parameters (see equation (3) in the main text) we need to calculate the partial derivatives of
 120 the expressions given with equation (S1.14a), and (S1.14b):

$$\frac{\partial d_{\perp}}{\partial V} = \frac{1}{\varepsilon_m^{-1} - \varepsilon_d^{-1}} \int_{-\infty}^{\infty} d\xi_{\perp} \frac{\partial}{\partial V} \varepsilon_{\text{LRA}}^{-1}(\xi_{\perp}, V), \quad (\text{S1.15})$$

$$\frac{\partial d_{\parallel}}{\partial V} = \frac{1}{\varepsilon_m - \varepsilon_d} \int_{-\infty}^{\infty} d\xi_{\perp} \frac{\partial}{\partial V} \varepsilon_{\text{LRA}}(\xi_{\perp}, V). \quad (\text{S1.16})$$

121 From here equation (5a) and equation (5b) in the main text follow immediately.

122 1.6 Surface-response functions and classical surface model

123 If we make the assumption that the perturbation caused by d_{\perp} component on the parallel component of the
 124 electric field is negligible (from equation (S1.8c) $\Delta\mathbf{E}_{\parallel} \approx \mathbf{0}$), then we can approximate $\Delta\mathbf{D}_{\parallel}$ as $\varepsilon_0(\varepsilon_d - \varepsilon_m)\mathbf{E}_{\parallel}$.
 125 Consequently, the expression for the perturbation of the surface current is

$$\Delta\mathbf{K} = i\omega\Delta d_{\parallel}\Delta\mathbf{D}_{\parallel} \quad (\text{S1.17})$$

$$\approx i\omega\varepsilon_0(\varepsilon_d - \varepsilon_m)\Delta d_{\parallel}\mathbf{E}_{\parallel}. \quad (\text{S1.18})$$

126 If we insert d_{\parallel} component perturbation Δd_{\parallel} from the main text, we obtain

$$\Delta\mathbf{K} \approx i\varepsilon_0 \frac{\omega_p^2}{\omega + i\gamma} \frac{\Delta\eta_0}{n_0} \mathbf{E}_{\parallel} \quad (\text{S1.19})$$

$$= \Delta\sigma_s \mathbf{E}_{\parallel} \quad (\text{S1.20})$$

127 This result is equivalent to one obtained from the classical surface model introduced by Bohren and Hunt (see
 128 equation (S1.2)).

129 1.7 Evaluating the d -parameters

130 Equation (9) in the main text involves an integral where the integrand depends on the inverse square of the
 131 local permittivity and the shape of the induced electron density. In order to address this, we conduct density
 132 functional theory (DFT) calculations using the "Jellium" approximation, which allows us to obtain electron
 133 densities as depicted in Fig. S1a. Specifically, we present the results for the case of $r_s = 3.18$ corresponding to
 134 bulk electron density of $n_0 \approx 5 \cdot 10^{28} \text{m}^{-3}$, as determined from a Drude model fit to the material data as discussed
 135 in SI section 1.3. To evaluate the integral, it is necessary to choose a spatially varying background permittivity
 136 $\varepsilon_b(\xi_{\perp})$. Deep inside the metal, it corresponds to the interband transitions contribution, $\varepsilon_{\text{bm}} = \varepsilon_m - \varepsilon_D$, where ε_D
 137 represents the Drude free-electron contribution. In the dielectric, it corresponds to the material permittivity ε_d .
 138 We adopt a smooth function that connects these two contributions, following the equilibrium electron density

$$\varepsilon_b(\xi_{\perp}) = n_0(\xi_{\perp}) \cdot \varepsilon_{\text{bm}} + (1 - n_0(\xi_{\perp})) \cdot \varepsilon_d. \quad (\text{S1.21})$$

139 Consequently, we obtain a smooth local permittivity ε_{LRA} , which is illustrated in Fig. S1b. The plot demon-
 140 strates a gradual transition from the permittivity of the metal to that of the dielectric. Due to the metal's
 141 significantly negative real part of permittivity and a small positive real permittivity of the dielectric, there exists
 142 a location where the real part of the local permittivity crosses zero. This specific region is denoted with a black
 143 rectangle in Fig. S1b and holds significance for the integral evaluation since the integrand contains the inverse
 144 square of the local permittivity, $\varepsilon_{\text{LRA}}^{-2}$, which we can restate as follows:

$$\frac{1}{\varepsilon_{\text{LRA}}^2} = \frac{(\varepsilon_{\text{LRA}}^*)^2}{|\varepsilon_{\text{LRA}}|^4}. \quad (\text{S1.22})$$

145 In Fig. S1c we present a zoomed-in view of the real and imaginary part of the local permittivity in the vicinity
 146 where epsilon approaches zero. Additionally, we show the absolute value $|\varepsilon_{\text{LRA}}|$ in Fig. S1d. It is evident that
 147 the absolute value of local permittivity exhibits an asymmetry with respect to the position of the minimum,
 148 denoted as $x_{\perp 0}$. Specifically, the values on the left side ($\xi_{\perp} < \xi_{\perp 0}$) are slightly larger than the values at
 149 equidistant locations on the right side ($\xi_{\perp} > x_{\perp 0}$). As a result, $|\varepsilon_{\text{LRA}}|^{-4}$ will exhibit a contrasting asymmetry,
 150 enhancing contributions from the right side of the peak position. Consequently, both the real and imaginary
 151 parts of the integrand, $\varepsilon_{\text{LRA}}^{-2}$, will exhibit the same asymmetry, as depicted in Fig. S1e. We determine the
 152 perturbation coefficient for the gold-glass interface and present it in Fig. S1 f. In the inset of the figure, we
 153 provide a logarithmic plot of the relative error η , showcasing the dependence of the real and imaginary parts
 154 of the perturbation coefficient on the size of the integration interval $\Delta\xi_{\perp}$ (illustrated in Fig. S1a), centered
 155 around the location of minimum $\xi_{\perp 0}$. It is apparent that in order to accurately determine the real value with
 156 a relative error of 10% or less, a relatively large integration interval, larger than 0.5 nm is required. On the
 157 other hand, the same error for the imaginary part can be achieved with an integration interval of approximately

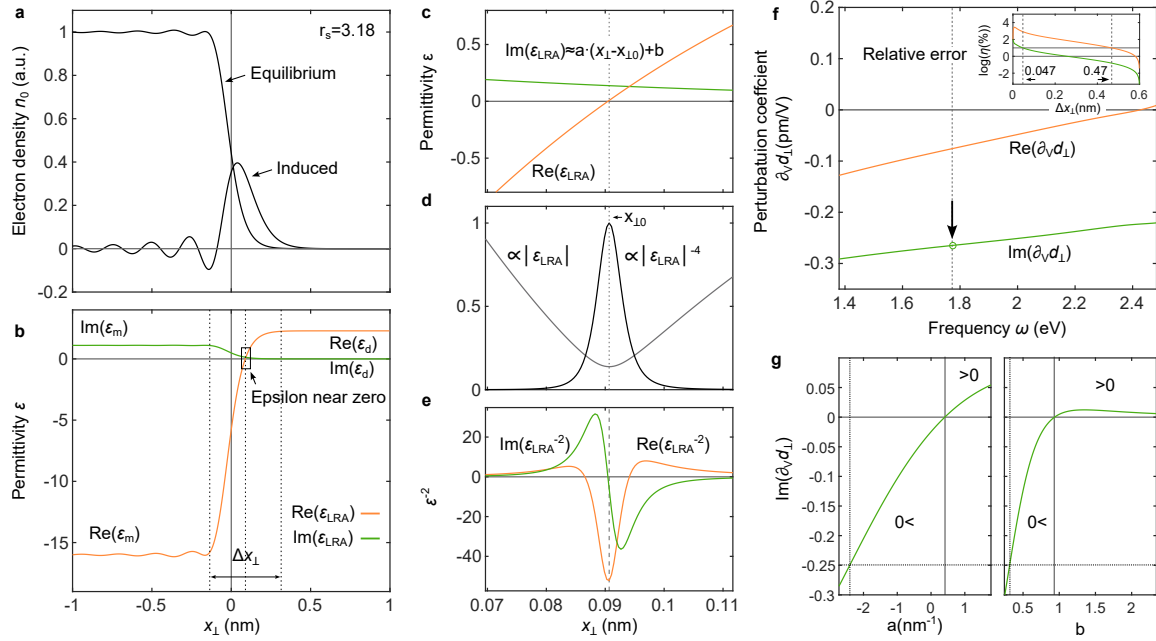


FIG. S1: **Evaluating the d_{\perp} perturbation coefficient.** **a**, Equilibrium and induced electron density for $r_s = 3.18$. **b**, Spatial dependency of local permittivity on gold-glass interface. **c**, Zoom-in region where local permittivity approaches zero denoted with black rectangle in **a**. **d**, Plot of absolute value of local permittivity and inverse of fourth power in epsilon near zero region. **e**, Real and imaginary part of square of inverse local permittivity in epsilon near zero region. **f**, Surface averaged perturbation coefficient of the d_{\perp} component. **g**, Influence of the imaginary part of local permittivity represented with line on the imaginary part of the perturbation coefficient with change introduced to line slope (left) and line y-intercept (right).

158 $\Delta\xi_{\perp} \approx 0.05$ nm. Therefore, the shape of the local permittivity within a relatively small spatial interval plays a
 159 crucial role in determining the imaginary part of the perturbation coefficient. To investigate this influence, we
 160 maintain the real part of the permittivity $\text{Re}(\epsilon_{\text{LRA}})$ as given by the model and assume that the imaginary part can
 161 be approximated by a linear equation, $\text{Im}(\epsilon_{\text{LRA}}) \approx a(\xi_{\perp} - x_{\perp,0}) + b$. In Fig. S1g, we illustrate the impact of the
 162 line slope, a (left), and the y-intercept, b (right), on the imaginary part of the perturbation coefficient. It can be
 163 observed that by increasing the line slope in a positive manner, the perturbation coefficient can be enhanced and
 164 rendered positive for $a > 0.3 \text{ nm}^{-1}$. Similarly, a positive perturbation coefficient can be achieved by increasing
 165 the y-intercept past the value of 0.9. This can be understood as introducing a change in asymmetry to the
 166 absolute value of local permittivity which is then translated to real and imaginary part of the inverse square of
 167 the permittivity.

168 1.8 Nanoresonator on a substrate

169 When dealing with a realistic geometry, such as a rectangular nanoresonator on a glass substrate (as depicted
 170 in Fig. S2a), the distribution of the induced surface charge $\Delta\eta_0(\mathbf{r}_s, V)$ is not uniform. In order to determine the
 171 response of such a system, we utilize finite element method (FEM) simulations and solve Maxwell's equations
 172 in a two-step procedure using commercially available numerical solver COMSOL Multiphysics. In the initial
 173 step, we solve for the static electric field and the induced surface charge density. Subsequently, we conduct
 174 simulations at optical frequencies. The simulation geometry consists of a sphere with a radius r_{sur} of 400 nm
 175 and a layer with a thickness t_a of 200 nm. This layer serves as the infinite element domain (IED) for electro-
 176 static simulations and the perfectly matched layer (PML) for optical simulations. In Fig. S2b, we present the
 177 geometry of the nanoresonator, which closely resembles the structures realized in the experimental setup. The
 178 nanoresonator's dimensions are as follows: length (l) = 140 nm, width (w) = 80 nm, and height (h) = 50 nm.
 179 Due to employed fabrication procedure, it is surrounded by a trench with a depth (t_d) of 40 nm and a width
 180 (t_w) of 50 nm (similar to Ref. [12]). Consequently, it stands atop a glass pedestal with a total height (p) of

181 50 nm. The single resonator exhibits a dipolar mode, as evidenced by the simulated radiation pattern (see inset
 182 of Fig. S2c). The peak position occurs around 1.7 eV, and the FWHM is roughly 280 meV. As in the experiment
 183 we solely observe light scattered above the critical angle, we conducted calculations to confirm that the shape
 184 of the resonance remains unaffected by the measurement procedure. To this end we compared the scattered
 185 power above the critical angle to the total scattered power (see Fig. S2c).

186 In the case of electrostatic simulations, the surface of the nanoresonator is assumed to be an equipotential,
 187 with an electric potential V , while a reference potential V_{ref} (ground) is positioned at an infinitely far distance
 188 by employing the IED. The dielectric constant of the glass κ_{glass} is set to 5, which falls within the typical range
 189 for glasses (from 5 to 10). This enhances the capacitance at the interface between gold and glass. At the corners
 190 of the nanoresonator, the static electric field reaches values of 0.35 GV/m, while the average induced surface
 191 charge density amounts to 2.7 mC/m². By integrating the induced charge density over the nanoresonator's sur-
 192 face for an applied potential of 10 V, the total induced charge is approximately 0.1 fC. This charge is equivalent
 193 to removing approximately 700 electrons from the nanoresonator's surface, resulting in a total self-capacitance
 of the system of around 10 aF. For our optical simulations, we use the Olmon SC material data for gold, which

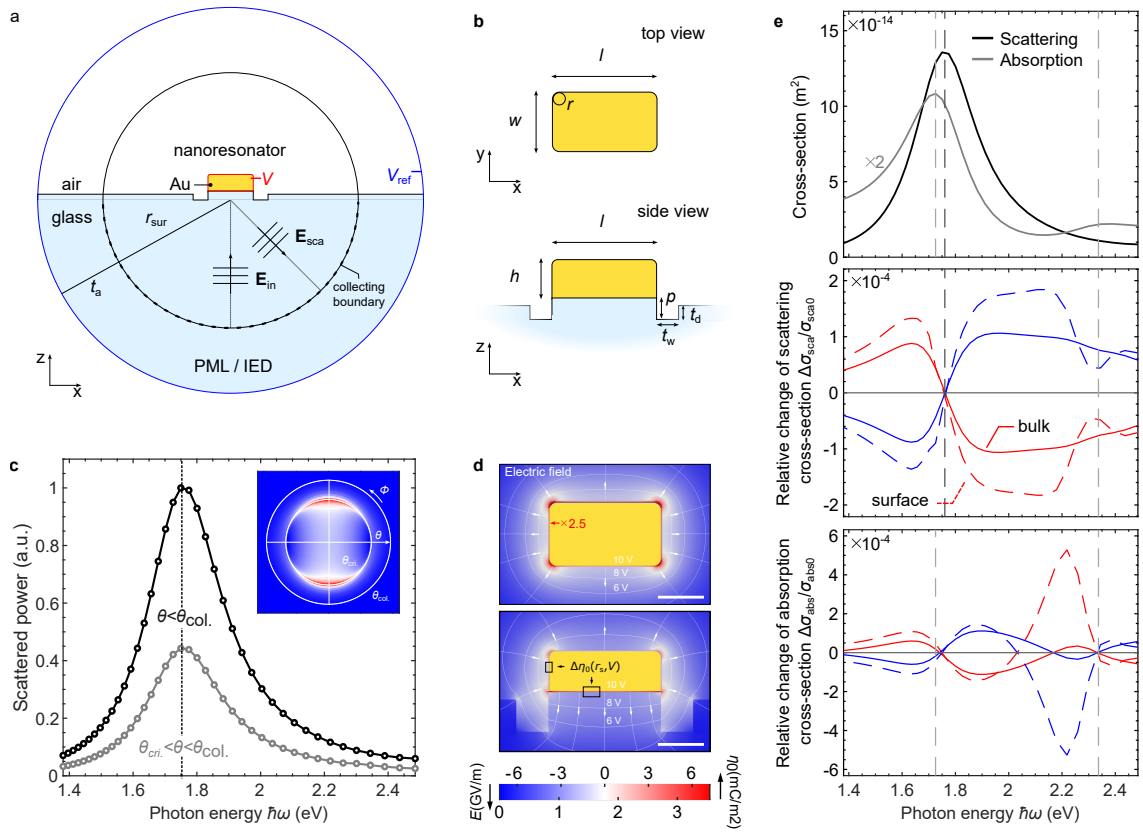


FIG. S2: **Electrically charged nanoresonator on a glass substrate.** **a**, The side view of the complete simulation geometry. In the electrostatic simulations, surface of the structure is an equipotential on a potential V , while the reference potential V_{ref} , situated on the outer surface of the IED, is set to zero volts. The structure is excited from below at a zero angle, using a plane wave characterized by the electric field \mathbf{E}_{in} . The light scattered by the structure is carried by the scattered electric field \mathbf{E}_{sca} , collected at the bottom hemisphere. **b**, Geometry of the nanoresonator. **c**, The simulated scattering spectra are obtained by integrating the scattered power over specific regions of the hemisphere through radiation pattern calculations. The inset illustrates a radiation pattern. **d**, Results of electrostatic simulations. Electrostatic field and induced surface electron density. **e**, (top) The absorption and scattering cross-section are presented. (middle) The relative change of the scattering cross-section. (bottom) The relative change in absorption cross-section.

194 we fit using a plasma frequency of $\hbar\omega_p = 8.3$ eV and collision time of $\tau = 14$ fs. The considered spectral range
 195

196 spans from 0.5 eV (2500 nm) to 1.24 eV (1000 nm), where the free electron response dominates. Due to the
 197 dependence of the plasma frequency on both the free electron density and effective mass, it is not possible to
 198 obtain the exact value for the unperturbed bulk density n_0 of the system. However, assuming that the effective
 199 mass of the electron is equal to the rest mass of an electron $m = m_e$, the unperturbed free electron density is
 200 $n_0 \approx 5 \cdot 10^{28} \text{m}^{-3}$. To examine the impact of the additional electrons, we apply both classical models. In the
 201 surface model, we introduce a surface current \mathbf{K} , with conductivity determined from equation (S1.13). This
 202 model is implemented in the numerical solver through the application of built-in boundary conditions for the
 203 tangential component of the magnetic field, as stated with equation (S1.3). The results for both models are
 204 illustrated in Fig. S2e. We observe a similar behavior in the relative change of scattering for both the bulk and
 205 the surface model, reaching values of approximately 1×10^{-4} on the resonance slopes, with no alteration in
 206 the resonance frequency. This pattern of the relative change is characteristic of a resonance-induced shifts (see
 207 Fig. 1a in the main text). Although the most significant change occurs near the resonance frequency, there are
 208 additional undulations in the relative change at around 2.3 eV. These changes are attributed to the presence of
 209 a dark mode, which is not clearly discernible in the scattering cross-section but is observable in the absorption
 210 cross-section.

211 1.9 Effect of the d -parameters on the properties of plasmonic resonance

212 A small interface averaged perturbation in one of the d -parameters $\langle \Delta d_i \rangle$, where $i = \{\perp, \parallel\}$, will induce a
 213 change in the scattering cross-section $\Delta_i \sigma_{\text{sca}}$. If we assume that each of the induced changes is smaller than
 214 the unperturbed scattering cross-section $\Delta_i \sigma_{\text{sca}} \ll \sigma_{\text{sca}}$, we can treat them independently. Therefore, the total
 215 change of scattering is given as the sum of the independent contributions

$$\Delta \sigma_{\text{sca}} = \sum_i \Delta_i \sigma_{\text{sca}}, \quad (\text{S1.23})$$

216 where the individual contributions are

$$\Delta_i \sigma_{\text{sca}} = \frac{\partial \sigma_{\text{sca}}}{\partial d_i} \langle \Delta d_i \rangle. \quad (\text{S1.24})$$

217 Additionally, we can express this change in terms of the influence on the eigenfrequency of the system as
 218 stated with equation (2) in the main text. Assuming a lossy harmonic oscillator as a model for a plasmonic
 219 nanoresonator relative change of the scattering cross-section near the resonance frequency can be modeled
 220 using the relative change of the Lorentzian

$$\frac{\Delta \sigma_{\text{sca}}}{\sigma_{\text{sca}0}} \approx \frac{\Delta L}{L_0}. \quad (\text{S1.25})$$

221 We can express this change analytically and use it as a fitting curve as analyzed in SI section 1.1 as follows:

$$\frac{\Delta L}{L_0} = \frac{\Delta L \omega_r}{L_0} + \frac{\Delta L \gamma_r}{L_0} = L_0 \left[2(\omega - \omega_r) \Delta \omega_r - \frac{\gamma_r}{2} \Delta \gamma_r \right]. \quad (\text{S1.26})$$

222 Therefore, for each of the d -parameters we can obtain its impact on the resonance frequency $\Delta \omega_r$ and resonance
 223 width $\Delta \gamma_r$ and retrieve the perturbation strengths $a_i = \Delta \tilde{\omega}_r / \langle \Delta d_i \rangle$.

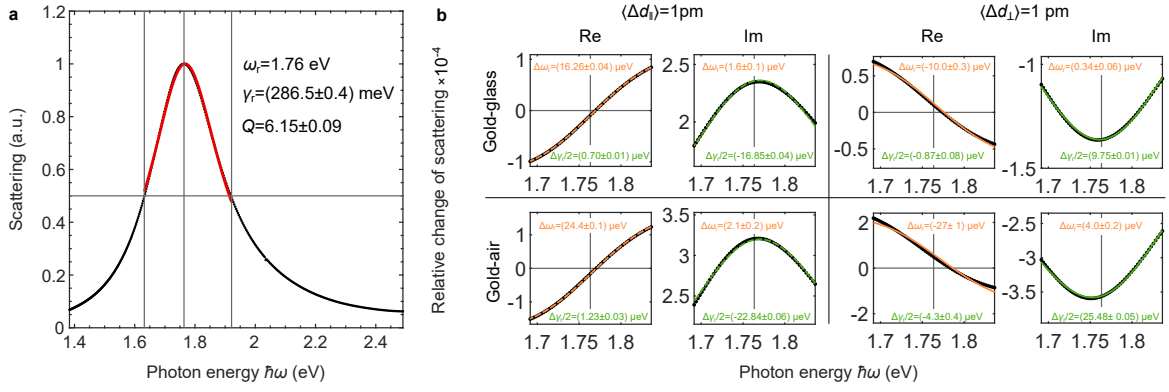


FIG. S3: **Influence of the d -parameter perturbations on the plasmonic resonance.** **a**, Scattering resonance (black) fitted with Lorentzian (red). **b**, Relative change of scattering fitted with relative change of Lorentzian for real and imaginary surface-averaged perturbations: left $\langle \Delta d_{\parallel} \rangle = 1 \text{ pm}$, right $\langle \Delta d_{\perp} \rangle = 1 \text{ pm}$, top gold-glass interface, bottom gold-air interface.

2 Experiment

2.1 Electro-optical setup

To measure the relative change of the scattering cross-section, we utilize an electro-optical setup, as depicted in Fig. S4. The setup is divided into two paths using a 50:50 beam splitter: the excitation path and the detection path. In the excitation path, we employ a tunable laser as the excitation source operating at the optical frequency ω . The laser light passes through a 300 μm pinhole which is then collimated using a lens positioned before the beam splitter. The iris is positioned before the beam splitter to remove the high-angle contributions. Therefore, a collimated beam is used to excite the structure, causing it to scatter light. The light reflected from the sample and scattered by the nanoresonator is guided through the detection beam path. Here, the reflected light is filtered out using a beam block. Additional filtering of the scattered signal is done by refocusing the scattered light to an intermediate image plane and using an iris to remove the stray light. The scattered light is then split using a 90:10 beam splitter, dividing the scattered light between the photodiode and the optical powermeter. The powermeter provides a direct readout, allowing us to obtain the unperturbed part of the scattered power P_0 . The signal from the photodiode is sent to a lock-in amplifier, enabling us to accurately measure the change in scattered power ΔP .

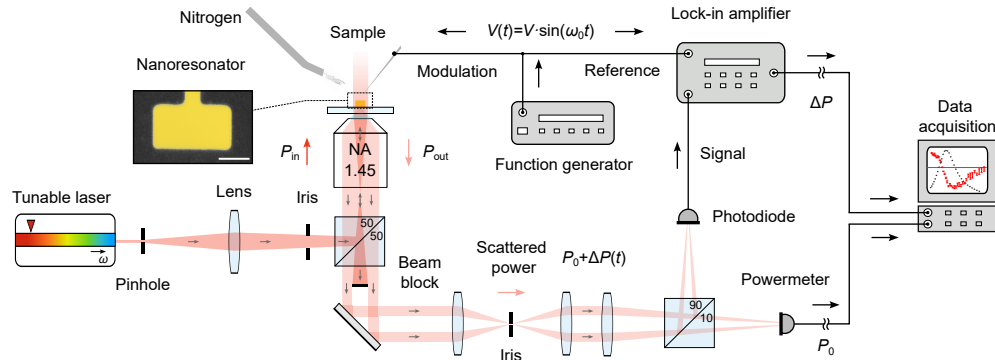


FIG. S4: **Experimental setup.** Schematics of electro-optical setup.

2.2 Scattering measurements

To determine the scattering cross-section, it is necessary to measure both the power scattered by the structure, P_s , and the excitation intensity, $I \approx P_{\text{in}}/r^2\pi$, where P_{in} represents the incoming power and r is the radius of the excitation spot. The typical beam size is approximately 1.5 μm , while the length of the longest nanoresonator is 180 nm. Therefore, it is assumed that the intensity is constant across the nanoresonator which justifies the use of a plane wave as an excitation source in simulations.

The nanoresonator is illuminated with light from the glass side, at angles below the critical angle. The power scattered by the nanoresonator P_s is measured by collecting the scattered light using the same objective that was used for excitation. The collection of light occurs at angles above the critical angle but below the maximum collection angle, which is determined by the numerical aperture (NA) of the objective.

To separate the light reflected from the sample from the scattered light, a circular patch is introduced in the back focal plane of the objective in the detection beam path. This circular patch effectively removes the reflected light. However, it is important to note that a small background signal persists due to the presence of stray light and scattering of light on imperfections present on the substrate. Consequently, the total scattered power, denoted as P , can be expressed as the sum of the power originating from the nanoresonator structure P_s , and the background scattered power P_b (see Fig. S5). Background signal is filtered out by focusing the light onto an intermediate plane and implementing an iris to eliminate scattering sources that are not in the proximity of the nanoresonator. To evaluate the impact of the residual background resulting from other scattering sources, we conduct measurements on a flat glass substrate while keeping the beam block in position. By measuring

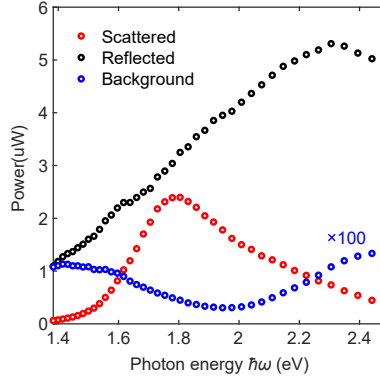


FIG. S5: **Measured scattered power.** Power of scattered signal (red), reflected signal (black) and background signal (blue).

the signal under these conditions, we observe that the background power is negligible compared to the power scattered by the nanoresonator structure – it accounts only for a few percent of the total scattered power as shown in Fig. S5, indicating that $P_s \approx P$.

In order to determine the incoming intensity I , we begin by measuring the power of light that is reflected from a flat glass substrate, denoted as P_r , in the absence of the beam block. Assuming that the reflectance R remains constant across the spectral range, the incoming power can be determined up to a constant factor R as $P_r = RP_{in}$.

2.3 Characteristics of the excitation source

Spatial shape

To characterize the excitation source both spectrally and spatially, we direct the beam reflected from the sample directly to the spectrometer. Initially, we measure the shape of the beam, as depicted in Fig. S6a. By fitting a Gaussian function to the beam profiles in both the x and y directions, which are passing through the intensity maximum, we extract the corresponding beam widths, r_x and r_y . These beam widths are expressed in pixels, as illustrated in Fig. S6b. To obtain the frequency dependent beam size, denoted as \bar{r} , we calculate the average of these two beam widths. Subsequently, we calculate the spectral shape of the average intensity, denoted as I , which is inversely proportional to the square of the beam size. It can be mathematically expressed as $I \approx CP_r/\bar{r}^2$. Therefore, the intensity and scattering cross-section are determined up to a constant factor C

$$S = C \cdot \sigma_{sca} \approx \bar{r}^2 \frac{P}{P_r}. \quad (S2.1)$$

We refer to S as scattering signal. As a result, the relative change in the scattering cross-section i.e. scattering signal is equal to the relative change of the scattered power, that is

$$\frac{\Delta\sigma_{sca}}{\sigma_{sca0}} = \frac{\Delta S}{S_0} \approx \frac{\Delta P}{P_0}, \quad (S2.2)$$

where P_0 unperturbed scattered power. This provides us with the possibility to relate experimental data directly to the model.

It is important to note that each of the measured quantities is influenced by the setup transfer function T_s . However, when we take a quotient of these quantities, the effects of the transfer function cancel out.

Spectral shape

In an ideal scenario, it would be preferable to employ an excitation source, centered at frequency ω , with a zero spectral line width to precisely investigate the response of the nanoresonator at this optical frequency. However, in our setup, the excitation laser exhibits a non-zero spectral line width, as depicted in Fig. S6c.

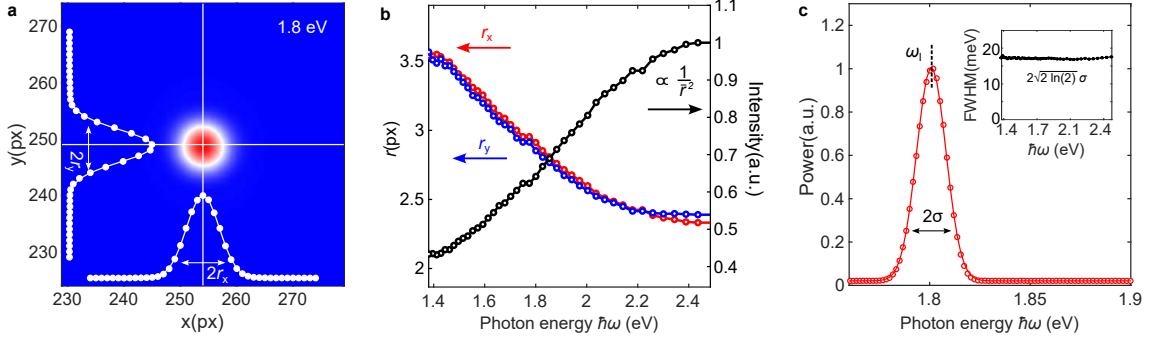


FIG. S6: **Characteristics of the excitation source.** **a** An image of the excitation beam is captured at 1.8 eV, after it reflects from a glass substrate. The image shows the beam profiles in the x and y directions. Gaussian curves are fitted to these profiles to determine the beam shape. **b** The beam sizes in the x and y directions are measured for different excitation frequencies. The average of the two beam sizes is used to calculate the intensity of the excitation source. **c** The source spectrum is obtained for a frequency of 1.8 eV. A Gaussian curve is fitted to the spectrum to determine the spectral line width. The spectral line width, is plotted as a function of the excitation frequency in the inset of the figure.

285 This introduces spectral distortion in the measurements due to the convolution of the true scattering cross-
 286 section and the intensity given by a Gaussian function $I_G(\omega; \omega_1, \sigma) = I(\omega) \cdot G(\omega; \omega_1, \sigma)$, where ω_1 represents
 287 the peak position and σ represents the width of the Gaussian function. Consequently, the measured power will
 288 be affected by this spectral distortion

$$\begin{aligned}
 P'(\omega) &= (\sigma_{\text{sca}} * I_G)(\omega) = \int_{-\infty}^{\infty} \sigma_{\text{sca}}(\omega') \cdot I(\omega') \cdot G(\omega'; \omega, \sigma) d\omega' \\
 &= \int_{-\infty}^{\infty} P(\omega') \cdot G(\omega'; \omega, \sigma) d\omega' = (P * G)(\omega),
 \end{aligned}
 \tag{S2.3}$$

289 and to retrieve true scattered power $P(\omega)$ we need to deconvolute the measured signal. Figure S7 illustrates the
 290 scattering signal taking into account the excitation source characteristics. The plot presents two scenarios: one
 291 considering only the beam size (black circles) and another (blue line) considering both the beam size and the
 292 spectral line width. The results show that the beam size influences the shape of the calculated spectrum, while
 293 the spectral line width of the excitation source has minimal impact.

294 2.4 Exemplary lock-in measurements

295 It is expected that the charge effect observed in lock-in measurements will only manifest at the fundamental
 296 frequency ν_0 i.e. frequency of the driving signal. Additionally, the signal should remain constant across the
 297 entire spectrum up to a frequency determined by the RC time of the system. At sufficiently low frequencies,
 298 only the in-phase component should be present, exhibiting a linear relationship with the applied voltage. These
 299 expectations have been experimentally validated, as depicted in Fig. S8. In panel a), the relative change in the
 300 scattering spectrum, measured at a driving frequency of $\nu_0 = 24$ kHz with an applied voltage of 10 V, clearly
 301 exhibits a purely in-phase component. Furthermore, panel b) demonstrates the absence of a lock-in signal at
 302 the second harmonic frequency $2\nu_0$. Panel c illustrates the linear scaling of the lock-in signal with applied
 303 voltage for three different optical frequencies, indicated by black arrows in panel a). Finally, panel d) exhibits
 304 the spectral dependence of the observed signal at ν_0 for the same three spectral points as in panel c). It can be
 305 observed that the signal remains constant above across the spectrum.

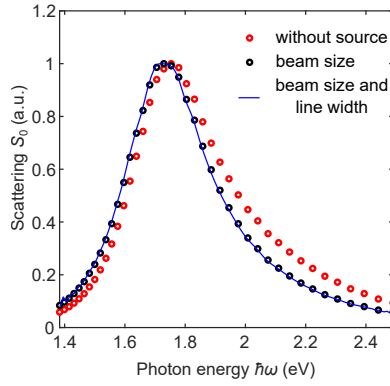


FIG. S7: **Measured scattering spectrum.** The scattering spectrum is plotted with and without considering the influence of the source characteristics. The red circles correspond to the measured spectrum without taking into account the source characteristics. The black circles represent the corrected spectrum, considering the non-constant intensity spectrum due to dispersive beam size. Additionally, the blue curve represents the spectral distortion caused by the non-zero linewidth of the excitation source.

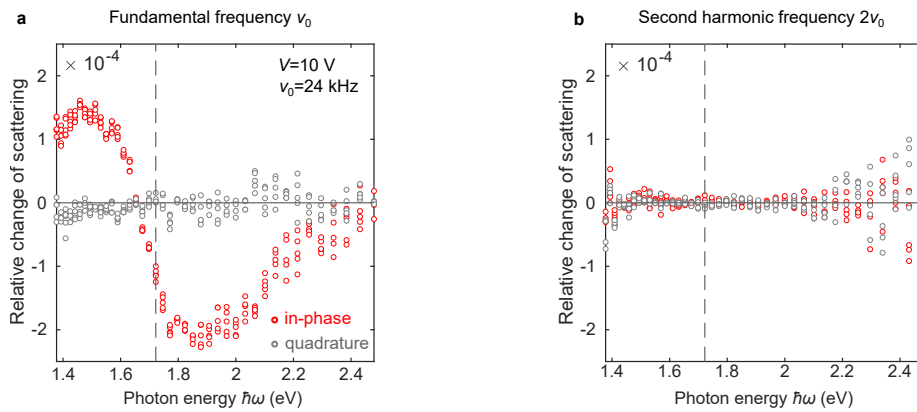


FIG. S8: **Exemplary lock-in measurements.** Spectral dependency of relative change of scattering for in-phase (red) and quadrature (gray) component for applied voltage of $V = 10$ V at **a**, driving(fundamental) frequency $\nu_0 = 24$ kHz and **b**, second harmonic frequency $\nu_0 = 2 \times 24$ kHz.

306 **References**

- 307 [1] Neil W Ashcroft and N David Mermin. *Solid state physics*. Cengage Learning, 2022.
- 308 [2] C. F. Bohren and A. J. Hunt. Scattering of electromagnetic waves by a charged sphere. *Canadian Journal*
309 *of Physics*, 55(21):1930–1935, 1977.
- 310 [3] T. Christensen, W. Yan, A.-P. Jauho, M. Soljačić, and N. A. Mortensen. Quantum corrections in nanoplas-
311 monics: shape, scale, and material. *Physical Review Letters*, 118(15):157402, 2017.
- 312 [4] P. J. Feibelman. Surface electromagnetic fields. *Progress in Surface Science*, 12(4):287–407, 1982.
- 313 [5] E. Hood and H. Metiu. Many-body phenomena at surfaces, edited by D. Langreth and H. Suhl, 1984.
- 314 [6] A. Varas, P. García-González, J. Feist, F. J. García-Vidal, and A. Rubio. Quantum plasmonics: from
315 jellium models to ab initio calculations. *Nanophotonics*, 5(3):409–426, 2016.
- 316 [7] P. J. Feibelman. Microscopic calculation of electromagnetic fields in refraction at a jellium-vacuum inter-
317 face. *Physical Review B*, 12(4):1319, 1975.
- 318 [8] R. C. Monreal, T. J. Antosiewicz, and S. P. Apell. Diffuse surface scattering and quantum size effects in
319 the surface plasmon resonances of low-carrier-density nanocrystals. *The Journal of Physical Chemistry*
320 *C*, 120(9):5074–5082, 2016.
- 321 [9] M. K. Svendsen, C. Wolff, A.-P. Jauho, N. A. Mortensen, and C. Tserkezis. Role of diffusive surface
322 scattering in nonlocal plasmonics. *Journal of Physics: Condensed Matter*, 32(39):395702, 2020.
- 323 [10] Y. Yang, D. Zhu, W. Yan, A. Agarwal, M. Zheng, J. D. Joannopoulos, P. Lalanne, T. Christensen, K. K.
324 Berggren, and M. Soljačić. A general theoretical and experimental framework for nanoscale electromag-
325 netism. *Nature*, 576(7786):248–252, 2019.
- 326 [11] N. A. Mortensen, P. A. D. Gonçalves, F. A. Shuklin, J. D. Cox, C. Tserkezis, M. Ichikawa, and
327 C. Wolff. Surface-response functions obtained from equilibrium electron-density profiles. *Nanophotonics*,
328 10(14):3647–3657, 2021.
- 329 [12] Jessica Meier, Luka Zurak, Andrea Locatelli, Thorsten Feichtner, René Kulloock, and Bert Hecht. Con-
330 trolling field asymmetry in nanoscale gaps for second harmonic generation. *Advanced Optical Materials*,
331 page 2300731, 2022.

